Timing landslide and flash flood events from SAR satellite: a ~~new~~ regionally applicable ~~method~~ methodology illustrated in African cloud-covered tropical environments

Axel A.J. Deijns[1,2,*], Olivier Dewitte[1], Wim Thiery[2], Nicolas d'Oreye[3,4], Jean-Philippe Malet[5], François Kervyn[1]

[1] Department of Earth Sciences, Royal Museum for Central Africa, 3080 Tervuren, Belgium
[2] Department of Hydrology and Hydraulic Engineering, Earth System Science, Vrije Universiteit Brussel, 1050 Elsene, Belgium
[3] Department of Geophysics/Astrophysics, National Museum of Natural History, 7256 Walferdange, Luxembourg
[4] European Center for Geodynamics and Seismology, 7256 Walferdange, Luxembourg
[5] École et Observatoire des Sciences de la Terre & Institut Terre et Environnement de Strasbourg, Centre National de la Recherche Scientifique, University of Strasbourg, F-67000 Strasbourg Cedex, France
[*] Corresponding Author. Email: axel.deijns@africamuseum.be

Abstract

Landslides and flash floods are geomorphic hazards (GH) that often co-occur and interact. They generally occur very quickly, leading to catastrophic socioeconomic impacts. Understanding the temporal patterns of occurrence of GH events is essential for hazard assessment, early warning and disaster risk reduction strategies. However, temporal information is often poorly constrained, especially in frequently cloud-covered tropical regions, where optical-based satellite data is insufficient. Here we present a ~~new~~ regionally applicable methodology to accurately estimate GH event timing ~~which~~ that requires no prior knowledge of the GH event timing, using Synthetic Aperture Radar (SAR) remote sensing. SAR can penetrate through clouds and therefore provides an ideal tool for constraining GH event timing. We use the open-access Copernicus Sentinel-1 (S1) SAR satellite that provides global coverage, high spatial resolution (~10-15 m) and a high repeat time (6-12 days) from 2016 to 2020. We investigate the amplitude, detrended amplitude, spatial amplitude correlation, coherence and detrended coherence time series in their suitability to constrain GH event timing. We apply the methodology on four recent large GH events located in Uganda, Rwanda, Burundi and DRC containing a total of about 2500 manually mapped landslides and flash flood features located in several contrasting landscape types. The amplitude and detrended amplitude time series in our methodology do not prove to be effective in accurate GH event timing estimation, with estimated timing accuracies ranging from a 13 day to a 1000 days difference. A clear increase in accuracy is obtained from SAC with estimated timing accuracies ranging from a 1 day to an 85 day difference. However, the most accurate results are achieved with coherence and detrended coherence with estimated timing accuracies ranging from a 1 day to a 47 day difference. ~~The GH event timing estimation accuracies vary among the GH events and the data products. Coherence and detrended coherence estimated timing accuracies range from a 1 day to a 47 day difference. The spatial amplitude correlation estimated timing accuracy ranges from a 1 day to an 85 day difference. The amplitude and detrended amplitude estimated timing accuracies range from a 13 to a 1000 day difference.~~ The amplitude time series reflect~~s~~ the influence of seasonal dynamics, which cause~~s~~ the timing estimations to be further away from the actual GH event occurrence

40 compared to the other data products. Timing estimations are generally closer to the actual GH event
41 occurrence for GH events within homogenous densely vegetated landscape, and further for GH events
42 within complex cultivated heterogenous landscapes. We believe that the complexity of the different
43 contrasting landscapes we study is an added value for the transferability of the methodology and
44 together with the open access and global coverage of S1 data it has the potential to be widely applicable.

1. Introduction

Landslides and flash floods are geomorphic hazards (GH) that can occur very quickly, sometimes in a matter of a few hours. GH frequently co-occur and interact (e.g. Rengers et al., 2016), they have a significant impact on the landscape (Petersen, 2001, Korup et al., 2010) and are severe threats for infrastructure and human life (Bradshaw et al., 2007, Kjekstad et al., 2009, Froude and Petley, 2018). Landslides and flash floods are often studied in isolation. However, it is their combined occurrence that can lead to more extreme impacts. For example, in 2013, several people were killed and ~7000 lost their homes in the Rwenzori Mountains in Uganda by a single debris-rich flash flood fed by upstream landslides (Jacobs et al., 2016a). Also, in 2011, a combination of flash flooding and mudslides across the highlands of the state of Rio de Janeiro claimed the lives of 916 people and left 35.000 people homeless (Marengo & Alves, 2012).

Understanding the temporal occurrence of GH events is essential for hazard assessment, early warning, and disaster risk reduction strategies (van Westen et al., 2008, Ali et al., 2017, Liu et al., 2018, Guzzetti et al. 2020). Temporal information with a few day accuracy is needed to understand the close association between precipitation and the occurrence of GH events (Guzetti et al., 2008; 2020, Turkington et al., 2014, Marc et al., 2018). For site-specific and local-scale investigation, this accurate information on the timing of GH events can be obtained with field-based approaches such as watershed/hillslope monitoring (Guzetti et al., 2012) or a network of observers (Jacobs et al., 2019, Sekajugo et al., 2022). However, when information on the timing of GH events is needed at a regional level, the acquisition of such data can only be achieved with satellite remote sensing (Joyce et al., 2009, Le Cozannet et al., 2020), especially in mountainous regions with difficult field accessibility and where monitoring and observation capacities are limited (Dewitte et al., 2021).

Satellite remote sensing, and more specifically the use of optical imagery, is a well-developed field of research to accurately determine the location of GH (Stumpf et al., 2014, Behling et al., 2014; 2016, Mohan et al., 2021). Optical-based satellite approaches can also be used for extracting the information on the timing of the GH events (e.g. Kennedy et al., 2018, Deijns et al., 2020), however such approaches are of limited use in cloud-covered environments, especially if temporal information with a few day accuracy is needed.

Synthetic Aperture Radar (SAR) satellite, being an active system with an ability to penetrate cloud cover, holds a great potential for characterizing the timing of GH. Additionally, the sensitivity of SAR satellite data to surface changes, including vegetation changes (Hagberg et al., 1995, Balzter, 2001, Barrett et al., 2012), soil moisture changes (Dobson & Ulaby, 1986, Dubois et al., 1995, Ulaby et al., 1996, Nolan & Fatland, 2003, Srivastava et al., 2006), and surface texture changes (Dzurisin, 2006) gives SAR the potential to display GH timing with an accuracy of days.

SAR derived products typically used for GH (event) analysis are ~~GH events are usually analyzed using SAR~~ amplitude data (i.e. changes in surface backscattering intensity of SAR signal between two images)

81 (e.g. Mondini et al., 2017; 2019, Esposito et al., 2020, DeVries et al., 2020, Handwerger et al., 2022)

82 for which amplitude correlation is a common method used in amplitude change detection (Mondini et

83 al., 2017, Konishi & Suga, 2018, Jung and Yun et al., 2020) ~~or~~ and ~~the interferometric~~the coherence

84 (i.e. the change in the ability of SAR wave fronts to stay spatially and/or temporally in phase between

85 the two images of an interferometric pair) (Burrows et al., 2019; 2020, Tzouvaras et al., 2020).

86 Additionally, there is a wide range of studies that use SAR-derived ground deformation to map landslides

87 (Casagli et al., 2017, Solari et al., 2020) or analyze pre-cursor movements (Intrieri et al., 2018) and

88 internal variability (Nobile et al., 2018). However, they are dependent on consistent high ~~interferometric~~

89 coherence values at the GH locations, which will make these methods of limited use in highly vegetated

90 landscapes (e.g. the tropics) (Komac et al., 2015; Solari et al., 2020) and for fast moving GH (e.g.

91 shallow landslides and flash floods) (Burrows et al., 2020; Tzouvaras et al., 2020). In recent GH

92 detection studies, amplitude products are usually preferred over coherence product~~s for GH detection~~s

93 (Ge et al., 2019, Jung and Yun et a., 2020, Mondini et al., 2021), since coherence generally yields less

94 accurate results due to lower resolution (Burrows et al., 2019; 2020) and ~~the~~a higher number of false-

95 positives (Aimaiti, 2019, Jung and Yun et al., 2020).

96 Despite the increasing use of SAR imagery for GH detection (Martinis et al., 2015, Twele et al., 2016,

97 Mondini et al., 2019, Psomiadis et al., 2019, Burrows et al., 2020, ~~Jacquemart and Tiampo, 2021,~~ Jung

98 and Yun, 2020, Tzouvaras et al., 2020, Jacquemart and Tiampo, 2021, Handwerger et al., 2022), to

99 date, only the recent study of Burrows et al. (2022) used SAR to refine the timing of GH inventories.

100 Although located in the tropics and showing accurate results, their study was only applied (1) within a

101 relatively densely vegetated landscape, (2) only on landslides, (3) using pre-processed amplitude

102 imagery with Google Earth Engine (GEE) (Gorelick et al., 2017), (4) with a-priori knowledge on the

103 timing of the event (i.e. the year)~~. and (5) without consideration of the effect of vegetation dynamics~~

104 ~~within the timespan. Since GH events often rarely occur in isolation when on a regional scale is~~

105 ~~considered~~GH events occur within a variety of landscapes (Emberson et al., 2020, Dewitte et al., 2021)~~.~~

106 Therefore, ~~there is a clear need to calibrate and validate any GH timing method for ~~a variety of~~varying

107 landscape~~s~~, and land use/land cover characteristics. Additionally, the frequent co-occurrence of

108 landslides and flash floods (Jacobs et al., 2016b, Rengers et al., 2016) warrants the need to analyze

109 them using a combined methodology. However, so far, there has never been research dedicated to their

110 combined temporal detection using radar satellite.

111 The Copernicus Sentinel-1 (S1) constellation is frequently used in GH detection studies (Mondini et al.,

112 2021). Next to the fact that it is freely available and acquired regionally (from 2016 onwards), it offers

113 a very good trade-off between frequency of acquisition (6/12 days) and spatial resolution (10-15 m

114 depending on the pre-processing parameters). These advantages make S1 an attractive tool to integrate

115 in a regional GH timing methodology.

116 In this study, we aim to develop a regionally applicable method~~ology~~ that automatically estimates GH

117 event timing using S1 SAR imagery on GH events spatially located, but with unspecified timing. We

analyze landslides and flash floods together as being co-occurring and interacting events. We create a methodology that can be applied at the regional scale in complex and various topographic and land use/land cover environments. The methodology is developed using ~~Focusing on different~~ four GH events either containing landslides, or a combination of landslides and flash floods located in contrasting landscape types observed ~~observed~~ within~~in~~ tropical Africa (see section 2.1). ~~, we~~We analyze an unprecedented amount of S1 SAR products, namely: ~~S1 SAR~~ amplitude, spatial amplitude correlation (a metric based on the common amplitude correlation) and ~~interferometric~~ coherence ~~changes~~. Specifically, we: (1) create S1 SAR time series and analyze their patterns and behavior at the location of several GH events, (2) demonstrate and assess the ability to detect the timing of GH events using changes within the S1 SAR time series and, (3) investigate the influences of the landscape characteristics on the ability to derive the timing from S1 SAR timeseries through a sensitivity analysis.

2. Data

2.1. Selection of GH events in a tropical region with diverse landscapes

We focus on the western branch of the East African Rift, a mountainous region with high population densities and diverse landscape and land use/land cover characteristics (Depicker et al., 2021a, Dewitte et al., 2021). The region has a bimodal precipitation distribution with two rainy peaks (October-November & March-April) and a main dry season (June-August) associated with the North-South migration of the Inter Tropical Convergence Zone (ITCZ) (Thiery et al., 2015, Nicholson 2017, Monsieurs et al., 2018a) with annual precipitation ranging from ~0.8m along the shores of Lake Tanganyika to easily more than 2m in the highlands, with the maximum in the Rwenzori Mountains (Monsieurs et al., 2020, Van de Walle et al., 2020). The seasonality of the precipitation strongly controls the occurrence of landslides and flash floods (Jacobs et al., 2016a; 2016b, Monsieurs et al., 2018a; 2018b, Kubwimana et al., 2021). Vegetation dynamics are high in the cultivated areas due to the variety of cropping practices (crop rotations and shifting cultivation, Heri-Kazi & Bielders, 2021). Moreover, the region is one of the most cloud-covered places in the world (Robinson et al., 2019) and a global hotspot of thunderstorm activity (Thiery et al., 2016; 2017, Peterson et al., 2021).

We investigate four GH events with known days of occurrence, and located in contrasting landscapes (fig. 1):

- Event 1 (Uganda GH event) is located in the southern part of the Rwenzori Mountains (Uganda) and counts 1063 landslide features of which some contribute directly to the sediment load of the valley river (fig. 1, Uganda). The event occurred between the 21st and the 22nd of May 2020. The terrain consists of pristine forests and some cultivated landscape (fig. 2a).

- Event 2 (Rwanda GH event) is located in the Karongi district (western Province, Rwanda) and counts 494 features composed of both landslide and flash floods and occurred on the 6th of May 2018 (fig. 1, Rwanda). The terrain consists of an inhabited and highly cultivated landscape with the presence of agricultural terraces (fig. 2b).

154   •   Event 3 (Burundi GH event) occurred around the hills of Nyempundu in the Cibitoke

155   region (north Burundi) and counts 318 features composed of landslides and flash floods and

156   occurred between the 4th and 5th of December 2019. Here, many landslides contribute directly

157   to the sediment load of the rivers (fig. 1, Burundi). The terrain consists of inhabited cultivated

158   landscape and sporadic tree cover (fig. 2c).

159   •   Event 4 (DRC GH event) occurred west of the city of Uvira (DRC), northwest of Lake

160   Tanganyika and counts 609 landslides and flash flood features that occurred between the 16th

161   and the 17th of April 2020. Many landslides are connected to the rivers where the flash floods

162   occurred. The debris-rich flash floods inundated parts of the city (fig. 1, DRC). The terrain is

163   characterized by an urban area, cultivated landscape, grassland, and sporadic tree cover (fig.

164   2d).
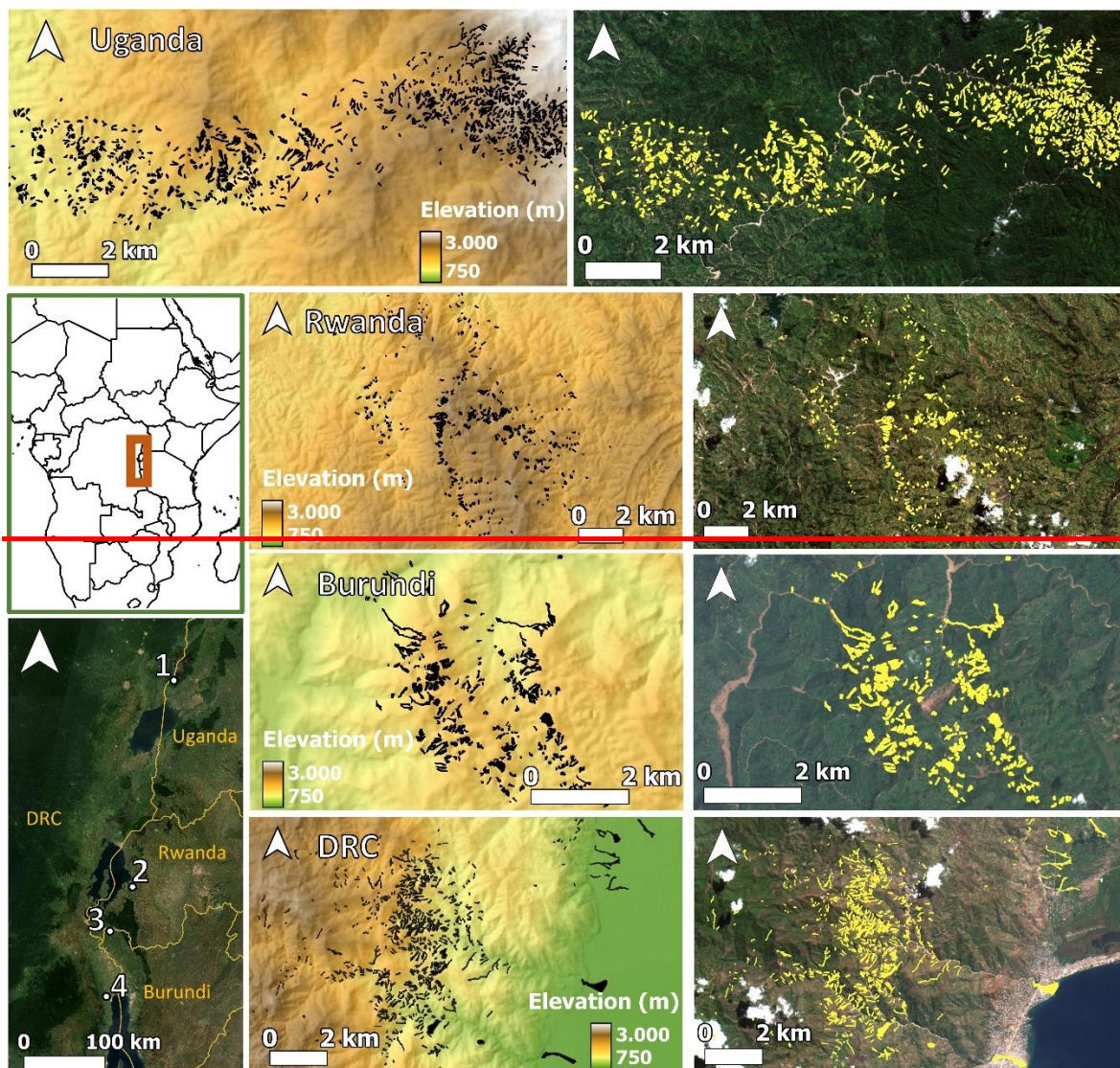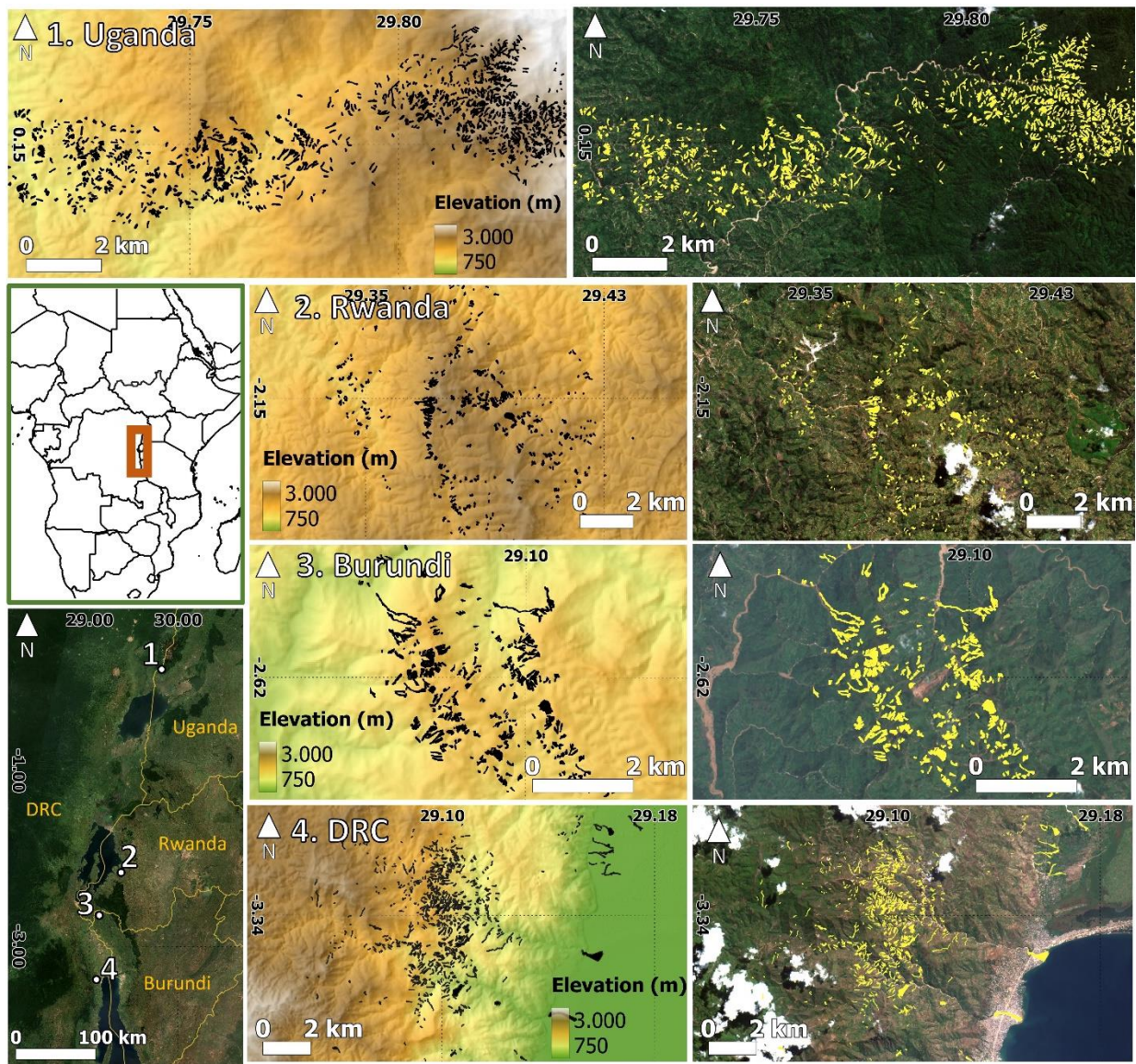
Figure 1. The location of the four GH events with their topographic (left: 30m ALOS 3D DEM, GH event features in black) and optical (right: S2 post-event image, GH event features in yellow) context. Note that in the close vicinity of the GH events of Uganda and Burundi, large sediment-loaded riverbeds are visible. This is a consequence of the GH events that contributed directly to the transport of extra material to the rivers, increasing not only their sediment content, but also their lateral mobility. These river dynamics are not included in our analysis. The two panels at the lower left depict the location of the GH sites (S2 imagery). Image credit: Contains modified Copernicus Sentinel data (2022), processed with Google Earth Engine. ALOS 3D DEM data provided by Japan Aerospace Exploration Agency (JAXA).

The locations of the GH events (fig. 1) are derived using the Copernicus Sentinel-2 (S2) Multispectral Instrument (MSI), high resolution (10m), high frequency (6 -12 days) satellite imagery. We manually digitized all individual features~~events~~ from the first available cloud-free S2 image after the event and a cloud-free S2 image with similar vegetation characteristics (compared to the post-event image) before the event. ~~We use PlanetScope Ortho Scenes (Planet Team, 2017) for validation of the GH event

180   inventory with a higher resolution satellite image. Planet operates with a constellation of multiple small

181   satellites producing very-high resolution (3m), high frequency (up to 1 day) imagery (Table 1).

182   *Table 1: Images information of manual mapping and dating GH events. Planet images are of the type*

183   *PlanetScope Ortho Scene (POS)*

GH Event	Sentinel-2				Planet	
	Date – pre	Date - post	Tile	Type	Date	Type
Uganda	2019-08-16	2020-06-01	35NRA	L1C	2020-06-29	POS
Rwanda	2018-03-09	2018-06-12	35MQT	L1C	2019-12-07	POS
Burundi	2019-08-06	2020-01-23	35MQT	L1C	2018-06-12	POS
DRC	2019-07-02	2020-06-06	35MQS	L1C	2020-10-06	POS

184   We prefer the use of Planet and S2 over the Maxar or the Spot/Pléiades images visible in Google Earth

185   because of the consistency in temporal and spatial resolution. To note, the Burundi GH event has

186   recently been mapped by Emberson et al. (2022) by means of a semi-automated method followed by a

187   manual correction using S2 satellite data. We expect our manually mapped Burundi GH event inventory

188   to be similar or more accurate since we use a combination of S2 and Planet satellite data and a

189   completely manual detection workflow. The date of GH event occurrences is determined from local

190   media and field observations, and if not available from these resources, determined by the first- and

191   last available imagery from S2 and Planet imagery.

192
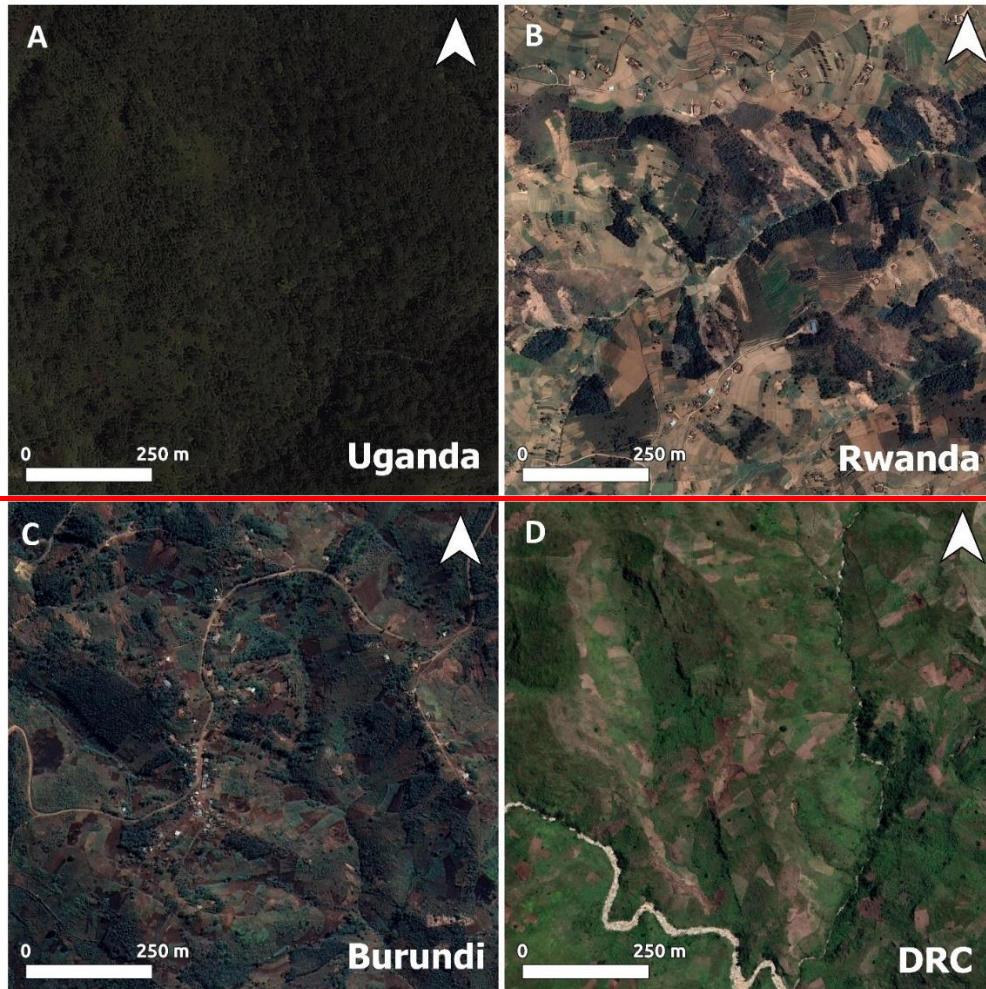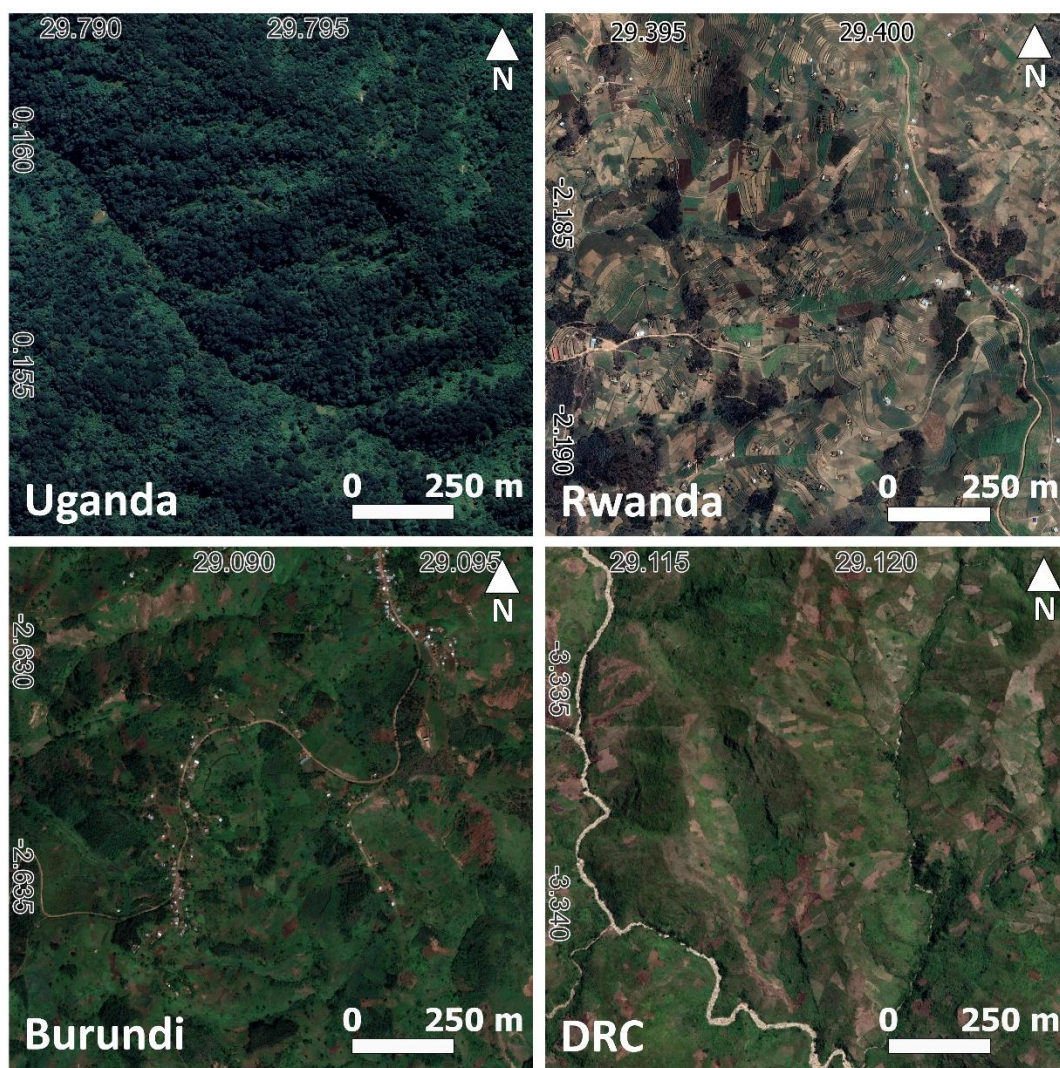
Figure 2. : Close up of the contrasting typical landscapes of the four GH events. ~~Coordinates at image center (lat, lon): (a) 0.144°, 29,757°, (b) -2.171°, 29.410°, (c) -2.635°, 29.090°, (d) -3.339°, 29.119°.~~ Maps Data: Google, ©2022 Maxar Technologies (~~a,~~ c, d) Google, ©2022 CNES/Airbus (a,b).

2.2. SAR time series

SAR time series at the GH location are constructed using the Copernicus S1 Level-1 Single Look Complex (SLC) imagery acquired in Interferometric Wideswath (IW). The S1 satellite is side-looking (right) and operates both on the ascending (from South to North) and descending (from North to South) tracks within the C-band frequency. To study the four GH events (fig. 1) we use all available high resolution S1 imagery (~15x15 meter resolution) from January 2016 to January 2021 at the location of the GH event at tracks 174 (ascending) and 21 (descending). This equals to between 196 and 208 ascending and 120 and 193 descending ~~high resolution S1 images~~ images -per GH event, where images occasionally overlap more than one GH event. ~~(~15x15 meter resolution) ranging from January 2016 up to January 2021~~ with a repeat time of six to twelve days with more consistently six days towards recent times. We use both amplitude and coherence information. S1 images over the study area are provided in vertical-vertical (VV) and vertical-horizontal (VH) polarizations. Different polarizations result

209 in different backscattering values (Shibayama et al., 2015, Psomiadis, 2016, Park & Lee, 2019, Burrows
210 et al., 2022). Mondini et al., 2019 noted a better definition of landslide-induced changes in vegetated
211 areas using the VH channel. In contrast, Burrows et al. (2022) found VV to perform better than VH for
212 landslide event timing estimation. Psomiadis (2016) concluded that VV polarization performed better
213 than VH polarization for flash flood mapping. Finally, VV polarization images are acquired more
214 consistently at the locations of our GH events. We therefore decide to use VV polarization for our
215 analysis. Due to the side-looking nature of the S1 satellite it is subjected to foreshortening, layover, and
216 shadowing which are SAR inherent quality problems that are amplified within mountainous regions and
217 affect image quality (Hanssen, 2001, Dzurisin, 2006). GH inventories are masked for foreshortening,
218 layover, and shadow areas to remove the individual landslides and flash floods that fall within these
219 inherently noisy areas.

2.3. SAR controlling factors

221 SAR amplitude and coherence are influenced by local slope angle (Hanssen 2001), soil moisture (Ulaby
222 et al., 1996, Scott et al., 2017), vegetation (Balzter, 2001, Barrett et al., 2012), and terrain roughness
223 (Dzurisin, 2006). Coherence is additionally influenced by atmospheric changes (Rocca et al., 2000) and
224 due to the use of image pairs, also by the temporal baseline (time between acquisition of two images),
225 the perpendicular baseline (distance between the location of acquisition of two images) and the
226 difference in incident angle of the paired images (Hanssen, 2001). Coherence values are generally very
227 low (high decorrelation) in densely forested areas due to constant movement of the leaves and stems
228 (Weydahl, 2001, Tessari et al., 2017), whereas bare soils or urbanized terrains, due to their static
229 nature, generally reveal relatively high coherence values (Colesanti & Wasowski, 2006). An increase in
230 coherence values after GH event occurrence is therefore expected. Amplitude values, on the other hand,
231 show to have a quite complex reaction to terrain change. Due to the influence of soil moisture and
232 roughness change on the amplitude values, the occurrence of a GH event could both increase and
233 decrease the amplitude values at the location of the GH event (Mondini et al., 2021, Burrows et al.,
234 2022). Both precipitation (in changing leaf- and soil wetness) and vegetation patterns, can dynamically
235 influence ~~SAR amplitude~~SAR amplitude and coherence values, causing a cumulative effect on the time
236 series (Srivastava et al., 2006, Brancato et al., 2017). This effect is more prominent over sparsely
237 vegetated areas due to geometric (vegetation growth and farming practices) and dielectric (moisture)
238 changes (Strozzi et al., 2000). Additionally, a change in atmosphere (precipitation events, ionospheric
239 disturbances) can dynamically influence the coherence values (Rocca et al., 2000, Jacquemart &
240 Tiampo, 2021). To better assess the ability to detect GH timing, it is essential to understand the dynamic
241 factors controlling the behavior of the signal.

242 We derive precipitation estimates from the GPM Level 3 IMERG Final Daily (10km spatial resolution)
243 dataset that has been validated through rain gauge data within the area (Nakulopa et al. 2022). General
244 vegetation patterns per GH event are visualized using the Normalized Difference Vegetation Index
245 (NDVI; Tucker, 1979). NDVI time series are derived from the Landsat-8 (30m spatial resolution) archive

246   and processed within the GEE environment We use the Landsat 8 atmospherically corrected surface
247   reflectance images provided within the GEE environment. We masked them for clouds using the quality
248   assessment band resulting from the CFmask algorithm (Foga et al., 2017).

249   We choose the lower resolution Landsat-8 over the higher resolution S2 imagery ~~to reduce~~to reduce
250   any unwanted local effects of NDVI change captured in the higher resolution S2 imagery, and since we
251   are only interested in the general vegetation trends within the area this should be sufficient. From the
252   cloud-masked images, a spatial-average NDVI time series is created spanning from 2016-2020 over the
253   undisturbed areas of the GH event area. The NDVI time series are further processed to monthly
254   averages, since we are interested in general vegetation patterns visible in the NDVI time series rather
255   than changes on smaller temporal timescales.

256   We use the ESA Climate Change Initiative Land Cover product (ESA, 2016) to categorize GH based on
257   their prior land cover to assess the influence of land cover on the timing detectability. This product has
258   been validated within the region by Depicker et al. (2021), showing an accuracy of 86.1 ± 2.1% in land
259   cover classification. All above mentioned factors are considered during the analysis of the SAR timeseries
260   and the GH event timing estimations.

261   **3. Methods**

262   **3.1. Sentinel-1 pre-processing**

263   The S1 images are pre-processed using the "InSAR automated Mass processing Toolbox for
264   Multidimensional time series" (MasTer) (Derauw et al., 2020, d'Oreye et al., 2021) processing chain (fig.
265   3, step 1). MasTer is a tool for automated SAR and SAR interferometry (InSAR) mass processing
266   (Samsonov & d'Oreye, 2012, Derauw et al., 2019; 2020, d'Oreye et al., 2019; 2021), that is incremental
267   (i.e. only computes the minimal required information when a new image is available) and optimized for
268   mass processing. The MasTer workflow is applied on both the ascending and descending track and
269   consists of:

270   (1) the application of orbit correction using the precise orbit files provided with the S1 data.

271   (2) The creation of time series of amplitude maps per track. Amplitude maps of each given track are
272   co-registered on a reference image taken from that track. Every amplitude image in the radar geometry
273   of that track is cropped and provided with the same grid and dimensions framing the area of interest.
274   Amplitude values are calibrated to sigma nought values. The amplitude images are multi-looked by a
275   factor 2 in azimuth and in range, to reduce speckle, leading to a roughly 28x5 m slant range resolution.
276   Radiometric terrain correction is applied to account for the local incidence angle variating with slope
277   angle resulting in amplitude values that are independent of slope angle (Small, 2011).

278   (3) The creation of coherence maps using consecutive images throughout the time series with a
279   maximum temporal baseline of 12 days and a maximum perpendicular baseline of 150 m. The coherence
280   maps are provided with the same multi-looking factor, grid, and ground range resolution as the
281   amplitude images.

282 (4) All the amplitude and coherence maps from all the tracks spanning a given GH area are geocoded

283 from slant range to ground range on a common grid with a 15 by 15 m resolution using the 30 m ALOS

284 Global Digital Surface Model. We decided to geocode the SAR imagery to make it compatible with all

285 our other data products and to allow for an easier visual comparison with optical imagery.———

3.2. Spatial amplitude correlation

287 We adapt the amplitude correlation approach, initially used for GH spatial detection (Mondini et al.,

288 2017, Konishi & Suga, 2018, Jung & Yun, 2020), to allow for GH timing detection at the location of the

289 GH event using the amplitude image stacks (fig. 3, step~~part~~ 2). We reason that the spatial correlation

290 is generally lost when the inter-pixel relationships between two images change at the location of a GH

291 event. Therefore, a significant change within the landscape such as a landslide or a flash flood will cause

292 a significant decorrelation. Due to the sensitivity of SAR amplitude to changes in vegetation (Balzter,

293 2001, Barrett et al., 2012), seasonal greening and browning trends have a pronounced influence on the

294 amplitude time series (Balzter, 2001, Barrett et al., 2012), which potentially limits the detectability of

295 the GH event within the time series. Since spatial correlation is only changing when the inter-pixel

296 relationships change, general trends that affect the entire area (lowering or increasing the SAR

297 amplitude values) do not influence the inter-pixel relationships (i.e. no spatial correlation change). Only

298 when significant inter-pixel change occurs, due to landslides or flash floods, the spatial correlation will

299 change. The spatial amplitude correlation (SAC) can therefore highlight the GH event occurrence within

300 the time series, while reducing the seasonal dynamics. To calculate the SAC, we use equation 1 that we

301 adapted from Jung & Yun (2020).

302 $$SAC_{x,y,poly} = \frac{\sum\{(A_{r,poly} - \overline{A_{r,poly}})(A_{x,poly} - \overline{A_{x,poly}})\}}{\sqrt{\sum\{(A_{r,poly} - \overline{A_{r,poly}})^2\}\sum\{(A_{x,poly} - \overline{A_{x,poly}})^2\}}} \quad x = date_1 \dots date_{N+1}; x \neq r \qquad (1)$$

303 with $SAC_{x,r,poly}$ the spatial amplitude correlation for the impacted area ~~(timing workflow 1: The complete~~

304 ~~GH event, timing workflow 2: per individual GH feature)~~ of date x in reference to date r, $A_{x,\ poly}$ the

305 amplitude pixels of impacted area _–at date x, and $A_{r,\ poly}$ the amplitude pixels of impacted area _–at

306 reference date r. Instead of calculating correlation between two subsequent images over a given

307 window, we calculate the correlation using one reference image (A_r) and all the other images within the

308 time series (A_x) using only the pixels within a designated impacted area (e.g. single GH feature or

309 complete GH event) ($_{poly}$). Consequently, every image within the amplitude image stack can be used as

310 a reference image and due to slight changes within every amplitude image this will inevitably result in

311 different SAC time series, one better highlighting the GH event than the other. We apply the equation

312 separately for ascending and descending images in a parallel workflow. Figure 4 shows schematically

313 how the SAC time series should behave using different reference images. Taking a reference amplitude

314 image before the GH event occurrence (fig 4a), results in high SAC before and low SAC after GH event

315 occurrence. The opposite is expected when using a reference amplitude image after the GH event (fig

316 4b).

317 We use every available image within the amplitude image stack as a reference image and calculated
318 the respective SAC time series from it. From here, it is necessary to identify the most appropriate
319 reference image.

320

321
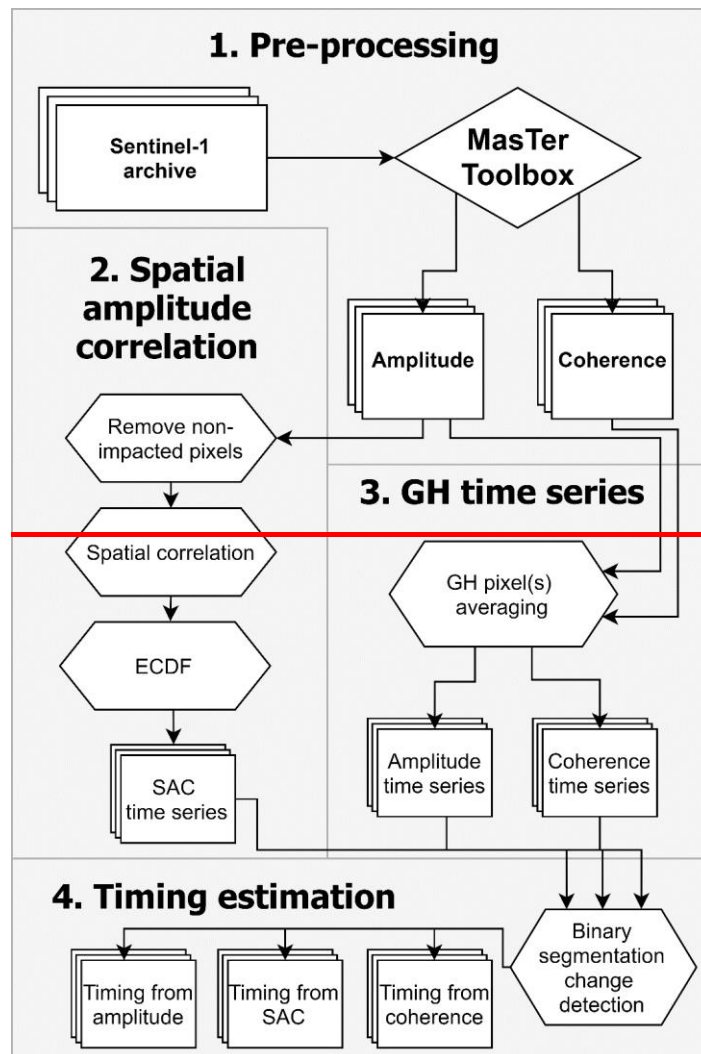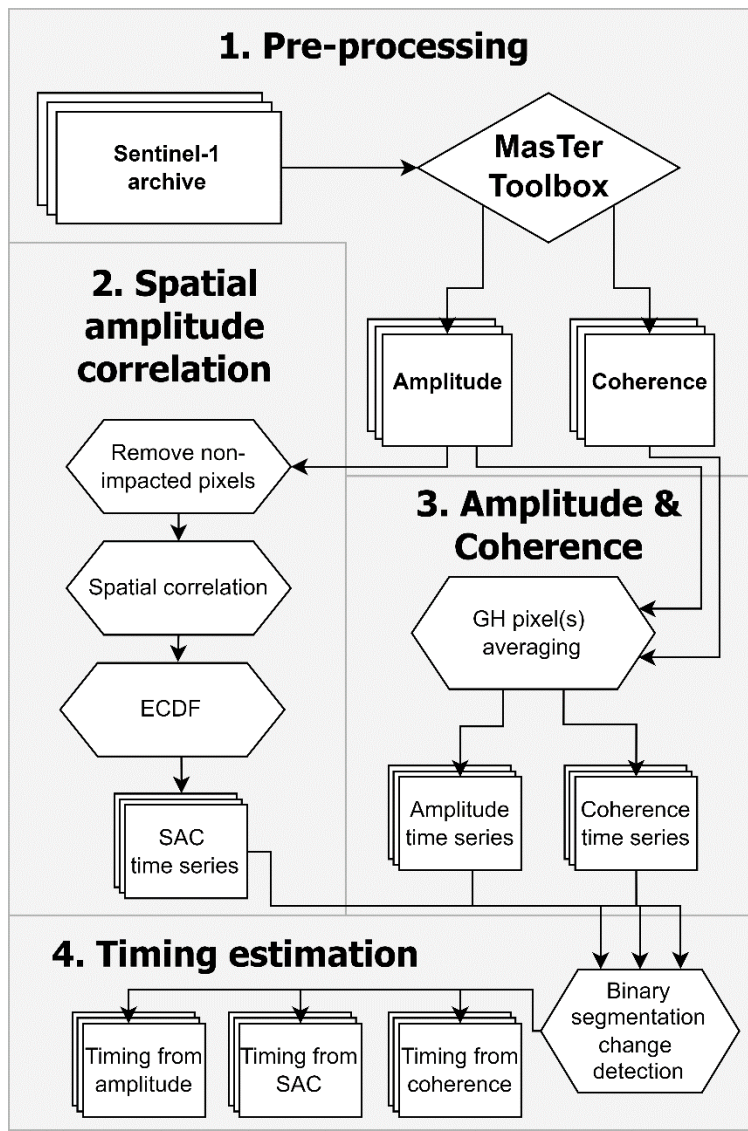
Figure 3. : ~~Workflow~~ Flowchart of the four-step methodology. Rectangles represent initial input imagery, output image stacks or time series products. The rhombus represents the external software product. Hexagons represent methodological steps, which are described in the text. (1) Pre-processing of the S1 imagery using the MasTer processing chain to acquire amplitude and coherence image stacks. (2) Application of the spatial amplitude correlation (SAC) method using Empirical Cumulative ~~Distibution~~Distribution Functions (ECDF) on the amplitude image stack resulting into SAC time series. (3) GH pixel(s) averaging for every image in the amplitude and coherence image stacks resulting into amplitude and coherence time series. (4) Application of binary segmentation change detection to acquire the date of the most significant change within the amplitude, SAC, and coherence time series.

Hence, we develop a new methodology that identifies the most suitable reference amplitude image by finding the SAC time series that most distinctively shows changes related to the GH event occurrence. We distribute every SAC time series as Empirical Cumulative Distribution Functions (ECDF) resulting in multiple ECDF curves equal to the amount of reference images. A SAC time series that contains a distinct change indicative of the GH event occurrence will show a similar distinct change in its ECDF.

336 Contrastingly, SAC time series that fail to distinctively highlight the GH event, ~~show an~~show an ECDF

337 that is similar to a normally distributed ECDF. Therefore, we create a normally distributed ECDF, using

338 the mean and standard deviation derived from the ensemble of ECDF curves, and identify the ECDF that

339 deviates most from it. Per ECDF we calculate and cumulate the difference from the normally distributed

340 ECDF. The ECDF with the highest cumulative difference is chosen as most representative and the related

341 SAC time series was used.

3.3. G~~eomorphic hazard~~H event ~~-~~timing estimation

343 GH event timing is determined on two scales within separate workflows:

- 344 Timing workflow 1: the complete GH event scale. ~~This workflow contains all pixels~~
  345 ~~encompassing the full GH event~~In this workflow, the steps outlined in figure 3 are carried out
  346 once using all pixels encompassing the full GH event.~~,~~ This result~~s in ing in one~~an ascending
  347 and one descending track time series for amplitude, SAC, and coherence.
- 348 Timing workflow 2: the individual GH scale. In this workflow, the GH event is subdivided in
  349 multiple individual GH features and the steps outlined in figure 3 are carried out separately for
  350 each individual GH feature.~~,~~ This ~~resulting~~results in multiple ascending and multiple descending
  351 track time series, equal to the amount of individual GH features, for amplitude, SAC, and
  352 coherence.

353 In both workflows we do not choose to remove fuzzy pixels (i.e., edge pixels that contain both impacted

354 and non-impacted landscape)~~,~~ s~~. S~~ince we do not know the effect of these pixels on the SAR time series

355 and GH event timing estimations. ~~, we apply the analyses without additional processing of the GH event~~

356 ~~inventories.~~ This allows us to establish baseline results. The ascending and descending track data are

357 processed separately throughout the two workflows. Amplitude and coherence time series are generated

358 by averaging the values within the identified impacted area per image (fig 3~~.3~~, step 3) and the SAC time

359 series are generated by applying the SAC method (fig 3~~.2~~, step 2;~~,~~ section 3.2) ~~on the same area~~within

360 both workflows ~~(workflow 1: the complete GH event, timing workflow 2: per individual GH feature)~~. The

361 resulting time series are normalized using the time series average to improve comparability.

362 Additionally, we make an effort to remove the seasonal influence and atmospheric effect on the

363 amplitude and coherence time series by subtracting the regional amplitude and coherence trend (i.e.,

364 time series) from the GH event scale amplitude and coherence time series (timing workflow 1). Both

365 precipitation events and seasonal vegetation dynamics are expected to cover the complete GH event

366 and its surrounding area. This detrending will therefore emphasize the change induced by the GH event

367 occurrence while removing any regional changes induced by either seasonal vegetation dynamics or

368 atmospheric effects (e.g. Jacquemart & Tiampo, 2021). The regional amplitude and coherence time

369 series are established by following ~~sections~~ step 1 and 3 ~~from~~ in the methodology flowchart (fig. 3),

370 using a larger area surrounding the GH events as input (i.e. a square of approx. 1.5 times the GH event

371 area, excluding the exact location of the GH event). This results in the detrended amplitude and

detrended coherence data products. ~~Given the fact that SAC is based on inter-pixel changes, subtracting a general value as a mean of detrending would make no difference. Moreover,~~ SAC is created to already consider seasonal vegetation dynamics so no additional detrending for this data product ~~was needed~~is performed.

We decide not to detrend individual GH feature time series (timing workflow 2), which ~~would~~ could include the use of a detrending buffer ~~such as in~~ (e.g. Burrows et al.~~,~~ ~~(~~2022). ~~S~~Since we deal with complex heterogenous land cover, proximate ~~landscape~~ land cover does not necessarily represent the ~~landscape~~ land cover at the ~~individual~~ GH feature, which prohibits from accurate detrending. Additional research ~~would~~ is ~~therefore be~~ required ~~to accurately~~before implement~~ing~~ such ~~such~~ a ~~detrending~~ method within~~method that is expected to be applicable in~~ a wide variety of environments.

Timing is ~~then~~ defined on every time series (for amplitude, SAC and coherence) using a binary segmentation change detection approach (Bai, 1997, Fryzlewicz, 2014) using the python package 'R~~r~~uptures' (Truong et al., 2020) (fig. 3, Step 4). The algorithm was set to predict only one breakpoint since we aim to detect the most significant change in the time series. The output of the applied binary segmentation change detection algorithm is a value that represents the location of an image within the image stack. The date of this image is extracted and assigned as the earliest date after the GH event occurrence. This applies for the amplitude and SAC time series. However, since coherence is based on image pairs, it would identify the image pair right after the GH event. We therefore assign the first date from this image pair as the earliest date after the GH event occurrence.

~~This allows us to locate, in time, the largest change within every time series.~~ On the complete GH event scale (timing workflow 1) this results in two dates (from ascending and descending track) per data product (amplitude, detrended amplitude, SAC, coherence, detrended coherence). On the individual GH scale (timing workflow 2), this results in several dates, equal to two times (one for ascending and one for descending track) the amount of individual GH features per data product (amplitude, SAC, coherence). Here we identify the ~~date that~~date that occurred most frequently (majority) as representing the timing of the event.

~~We expect that the coherence image pair that demonstrates an increase in coherence compared to the former coherence image pair consists of less vegetated terrain (as caused by the GH event) and thus contains post-event conditions (Tzouvaras et al., 2020, Burrows et al., 2020; 2021). The first date from this post-event coherence image pair is therefore extracted and defined as representing the timing of the event.~~ We define the minimal uncertainty in timing estimation by the difference between the estimated ~~image date~~date of occurrence and the date of the image ~~before that one within the image stack~~prior to that (i.e. a maximum of 12 days).
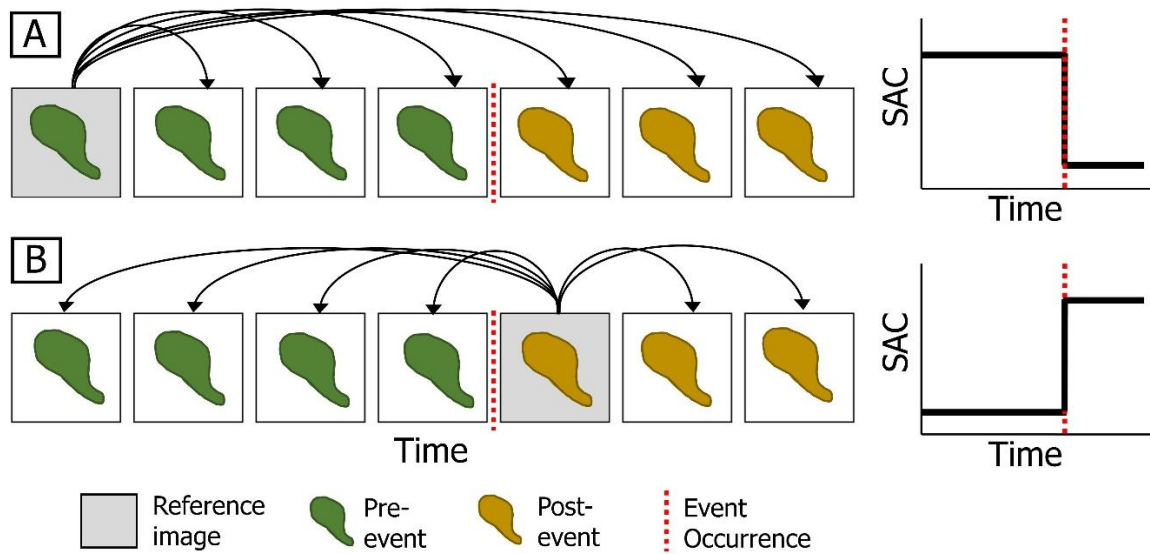
Figure 4. : Iidealized schematice of the SAC method using two2 different reference images: one before and one after the occurrence of the GH event (A, B). Squares represent images, the red dotted line indicates the occurrence of a GH event. Inside the images are the conditions of the impacted area (represented here as single GH feature but is similar for complete GH event). Pre-event conditions are displayed in green. Post-event conditions are displayed in brown. The black curved lines represent the combination of images on which equation 1 is applied to achieve the resulting SAC time series. The schematic SAC graphs (right) depict the expected results using a reference image before the event (A) with high correlation before and low correlation after the event, and using a reference image after the event (B) with low correlation before and high correlation after the event.

3.4. ~~Time series~~ Sensitivity analysis with respect to landscape characteristics

In ~~sS~~section 2.3 we discuss the controlling factors on the SAR signal. Here, we aim~~try~~ to understand the influence of these controlling factors plus the influence of individual GH properties on the detectability of the event timing. We carry out a sensitivity analysis on GH area (effect of a changing number of pixels/pixel mixing, Deijns et al., 2020), slope angle (change in image acquisition geometry, Zebker and Villasenor, ~~1992, Hanssen~~1992, Hanssen, 2001), land cover (changing vegetation and soil moisture patterns, Giertz et al., 2005), and slope aspect (different effect of layover, shadowing within ascending and descending track, Hanssen, 2001, Dzurisin, 2006). We carry out the analysis separately for the ascending and descending track images. Per individual GH feature we derive the average value of the above-mentioned parameters. We find more smaller-sized GH in the Rwanda GH event (fig 5a), a slight deviation (peak more to the left) in slope distribution for the Uganda GH event (fig. 5b) and a large variation in slope aspect distribution for different GH events (fig. 5d). Additionally, land cover distribution is different for every GH event (fig. 5c) which corroborates with what we see ~~on the satellite images~~ in (fig~~ure.~~ 2~~)~~.

429 The sensitivity analysis is carried out iteratively over every parameter from a minimum value to a
430 maximum value using predefined steps (Area: 1000 m², Slope: 5°, Land Cover: per individual land cover
431 type, Slope aspect: 45°). Per iteration the GH inventory is reduced to contain only individual GH features
432 that meet the iteration conditions. We exclude bins that contained less than 20 individual GH features
433 to avoid non-sense (very high or very low) values that would negatively influence the quality of the
434 trend.

435 Per bin-size, we calculate the timing ~~is calculated~~ for every individual GH feature, and the percentage
436 of timing estimates that fall within one month of the actual event occurrence over the total amount of
437 individual GH features ~~within that specific bin is calculated~~. Higher percentages indicate more timing
438 estimates closer to the actual event occurrence. The variations within this percentage are subsequently
439 analyzed to relate changing characteristic to performance.
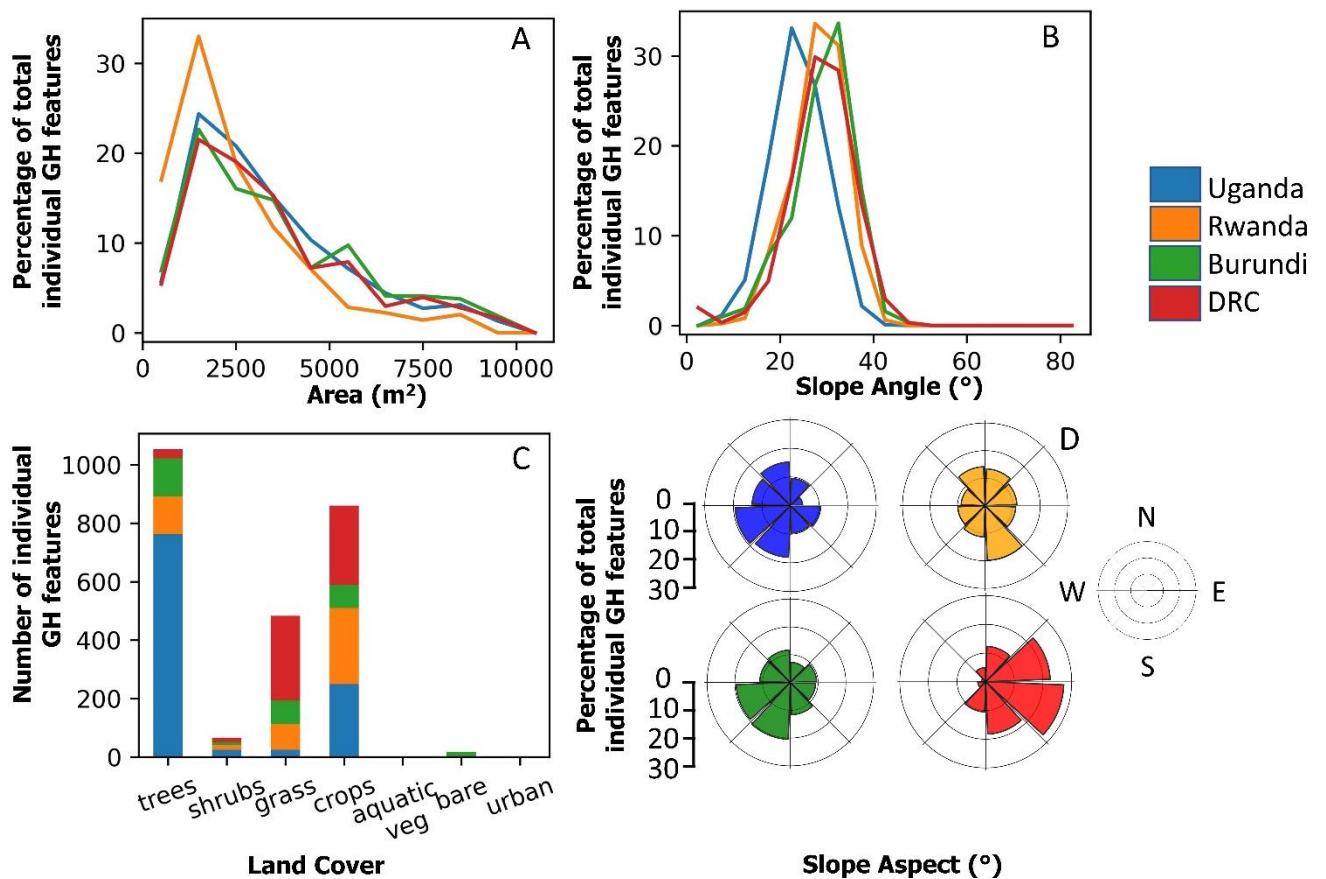
441 *Figure 5. P: p̶arameter distributions per GH event (Uganda, Rwanda, Burundi, and DRC). (A) Percentage*
442 *of individual GH ̶–over total amount of individual GH against area (m², bins of 1000 m². (B) Percentage*
443 *of individual GH over total amount of individual GH against slope angle, bins of 5°. (C) Number of*
444 *individual GH against land use/land cover. (D) Percentage of individual GH over total amount of*
445 *individual GH against slope aspect, bins of 15°.*

4. Results

4.1. ~~GH~~ Geomorphic hazard event time series

We created amplitude, detrended amplitude, SAC, coherence, detrended coherence time series for the four GH events in Uganda, Rwanda, Burundi, and DRC (location in fig. 1) and present it in figure 6 together with the average monthly Landsat 8 NDVI and IMERG monthly cumulative precipitation.

The distinctiveness of the GH event occurrence within the time series varies significantly per data product (fig. 6). SAC (fig. 6i-l) and coherence (fig. 6m-t) time series showcase the timing of the event with a significant change of value at the time of the event occurrence. ~~Change in coherence due to the GH event is clearly indicated by the increase in value starting from the post-event coherence pair.~~ A significant decrease ~~for~~ in the co-event (the coherence value from the pre- and post-event image) coherence ~~pair~~ is not visible.

The amplitude time series do not show any distinct change at the time of the GH event occurrence (fig. 6 a-h), except for the Uganda GH event (fig 6a,e). Particularly in the amplitude time series, and to a minor extent in the coherence time series, clear cyclicity can be observed, ~~which~~ that correspond~~s~~ with the two drier periods (December-February and June-August) that are prevalent in the region (Bonfils, 2012, Nicholson 2017, Monsieurs, 2018a). The NDVI shows seasonal correlation with the precipitation patterns, where NDVI patterns follow precipitation patterns with a short time lag (fig 6 u-x). Stronger NDVI variations align with a stronger cyclicity within the amplitude, SAC, and coherence time series which is particularly visible when comparing the Uganda GH event (weak amplitude SAC and coherence cyclicity, limited NDVI fluctuations) and the DRC GH event (stronger amplitude, SAC, and coherence cyclicity, large NDVI fluctuations). The cyclicity clearly influences ~~–~~ the distinctiveness of the GH event within the time series. When comparing the landscape of both GH events (fig. 2a,d) a sharp contrast is observed. The Uganda GH event region is mostly covered by forest, whereas the DRC GH event region is mostly covered by grass- and cropland. Consequently, we find that seasonal NDVI oscillations vary significantly from one study area to another given the difference in landscape. ~~The seasonal oscillations in vegetation are visible~~ are visible ~~within the amplitude and coherence timeseries and subsequently influence the distinctiveness of the GH event within these timeseries.~~

Time series detrending clearly reduces seasonal cyclicity within the time series, which is particularly visible for the coherence time series (fig. 6q-t) and to a much smaller degree for the amplitude time ~~series (~~ series (fig. 6e-h). For example, the DRC GH event coherence time series benefits from this detrending procedure such that seasonal cyclicity is almost completely removed, ~~and in the resulting time series a sudden~~ leaving a distinct increase in coherence values after ~~can be observed after~~ the occurrence of the GH event (fig. 6t). Detrending ~~of~~ the amplitude time series shows ~~some improvements~~ a minor reduction in cyclicity, ~~but is remains difficult to~~ but the distinctiveness of the GH event within the time series remains ~~poor~~ low.

481

482
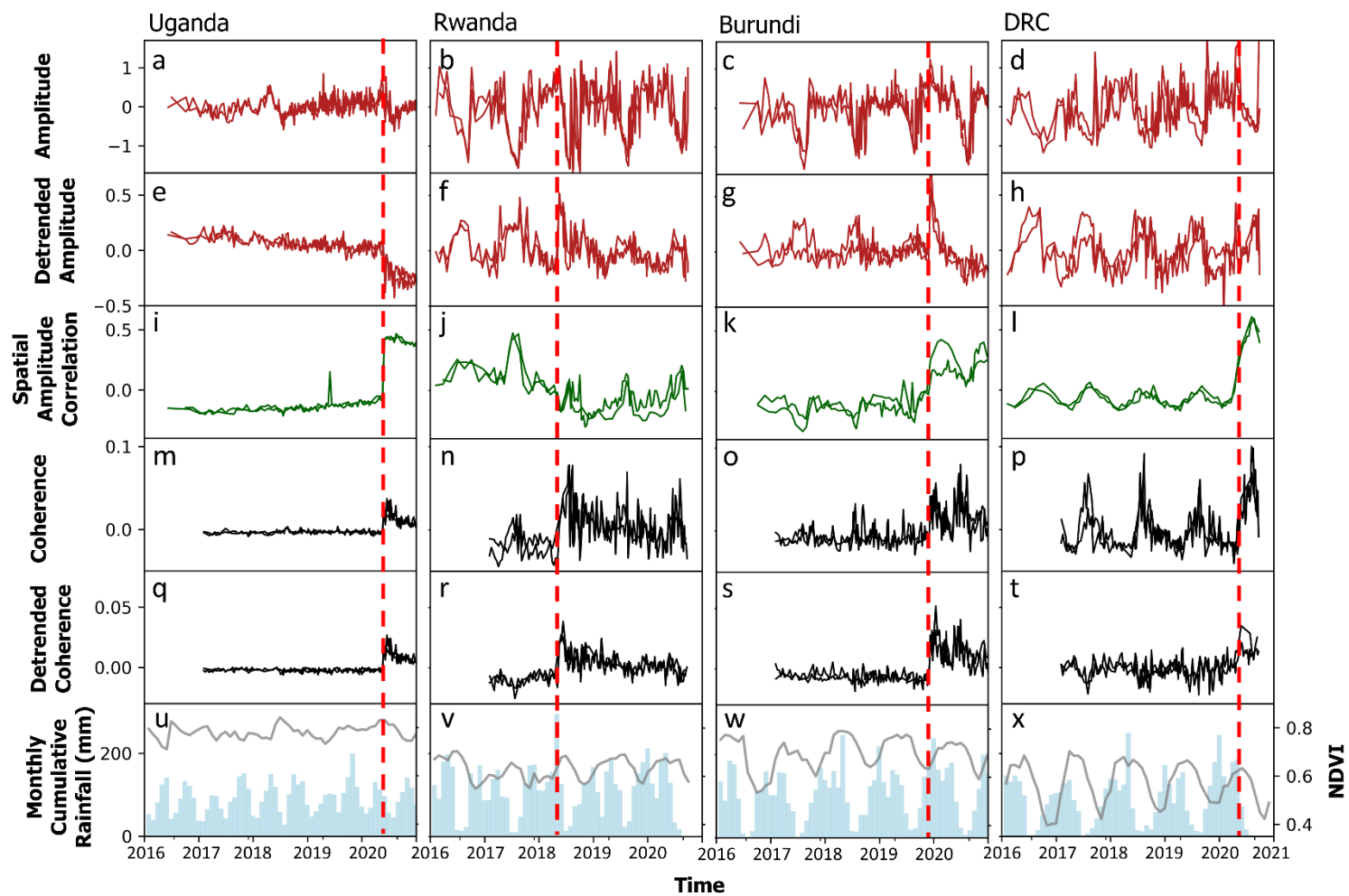
Figure 6.~~:~~ GH event (detrended) amplitude (red), spatial amplitude correlation (SAC, green) and (detrended) coherence (black) time series. The dashed red line represents the timing of the GH event occurrence within the time series. All coherence, amplitude and SAC time series show two lines of a similar color representing the ascending and descending track time series. The time series are created according to the complete GH event scale ~~method~~ workflow described in sections ~~3.2 (SAC) &~~ 3.3 ~~(amplitude and coherence)~~. The bottom row shows the monthly cumulative precipitation (light blue bars) from IMERG satellite data and the monthly averaged NDVI values (grey line) from Landsat 8 (method described in section 2.3).

4.2. Geomorphic hazard~~GH~~ event timing

Figure 7 shows the timing estimation at the GH event scale (timing workflow 1) from the (detrended) amplitude, SAC and (detrended) coherence time series. The difference in days from the actual occurrence of the GH event is visualized by a ~~timing~~ range ~~(i.e.i.e., uncertainty in estimated timing, length of the bars in fig. 7) is defined by the minimum and maximum difference in days of the estimated timing from the actual GH event occurrence and takes into account the estimated pre-event image (or image pair for coherence), estimated post-event image (or image pair for coherence) and the actual GH event occurrence timing range~~that incorporates the minimal uncertainty in timing estimation (fig. 7 and fig. 8; see section 3.3). Timing e~~E~~stimation~~s~~ from the ~~the~~ amplitude time series ~~time series perform poorly~~generally have lower accuracies with estimated timing ranging from a 46 day difference (Uganda, descending) to a 1000 day difference (Uganda, ascending). Estimations from the SAC time series range between a 1 day (Uganda) and a~~n~~ 85 day (Rwanda) difference and estimations from the coherence time series range between a 1 day (Uganda) and a 47 day (Rwanda) difference. Highest accuracies are achieved with time~~s~~ series showing less seasonal fluctuation and a steep change at the time of event occurrence (fig. 5). Timing estimations from the detrended amplitude time series show an increased accuracy compared to amplitude time series with the most significant change for the Uganda GH event from a 46-1000 to a 13-22 day difference, but performance is still poor and generally useless for accurate timing estimation. Detrending the coherence time series increases timing estimation accuracy compared to the non-detrended coherence timing estimation for the DRC event (25-32 to a 1-5 day difference), but in general the estimations remain the same.

Figure 8 shows the timing estimation based on the individual GH features within the GH event (timing workflow 2). ~~Similar to figure 7, timing range (i.e.i.e., uncertainty in estimated timing, length of the bars in fig. 8) is defined by the minimum and maximum difference in days of the estimated timing from the actual GH event occurrence.~~ Here, the estimated timing represents the date that is estimated most frequently between all individual GH features (as explained in section 3.3). The percentage of individual GH features that estimate this (most frequently estimated) date over the total amount of GH features (%maj) are shown ~~is included~~in figure 8. ~~in figure 8.~~

In general, timing estimation from the amplitude time series ~~performs rather poorly~~have low accuracies with estimated timing ranging from a 13 day difference to an 831 day difference. A distinct increase in accuracy is seen for the Uganda GH event compared to the GH event scale (fig. 7)~~in estimated timing accuracy, compared to the results from the GH event scale (fig. 7, timing workflow 1), is seen for the Uganda GH event. But~~ However, the other GH events do not show any distinct increase in timing estimation accuracy. The %maj ranges between 13% and 32.4% and shows that for some GH events a large portion of the individual GH features estimate a date that is far from the actual date of the GH event occurrence. The percentage of individual GH features that estimate a date within one month of the actual GH event occurrence from amplitude time series is 24.2% (ascending) and 26.9% (descending) for the Uganda GH event, but much lower for the other GH events, corroborating the fact that the timing detection method performs poorly ~~with~~ for the amplitude data product.

Timing estimations from the SAC time series from individual GH features (fig. 8~~, timing workflow 2~~) differ compared to the timing estimations at the GH event scale (fig. 7~~, timing workflow 1~~). An increase in accuracy is seen for Rwanda (ascending) and DRC (ascending) and a decrease in accuracy for Burundi (ascending) and DRC (descending). The estimated timing ranges from a 1 day difference to an 85 day difference. Although estimated timing accuracy is higher for SAC compared to amplitude, %maj values are quite low, indicating weak estimations. The percentage of individual GH that estimate a date within one month of the actual GH event occurrence ranges from 0.2 (Rwanda, descending) to 38,1 (Uganda, descending). Exceptionally, for the Uganda GH event, %maj and estimated timing within one month of the GH event occurrence from the SAC time series is highest in comparison with amplitude and coherence (fig. 8).

Timing estimations from the coherence time series from individual GH features (fig. 8) are similar to those achieved at the GH event scale (fig. 7), and have, generally, the highest accuracy for all data products. The %maj values ranged from 13.5 (Burundi, ascending) to 38.4 (DRC, descending). The percentage of individual GH features that estimates a date within one month of the actual GH event occurrence ranges from 0 (Rwanda, descending) to 38,4 (DRC, descending). The low percentages from the Rwanda descending track can be attributed to the fact that the estimated date is 37 days from the GH event occurrence and therefore just falls outside the one-month threshold.
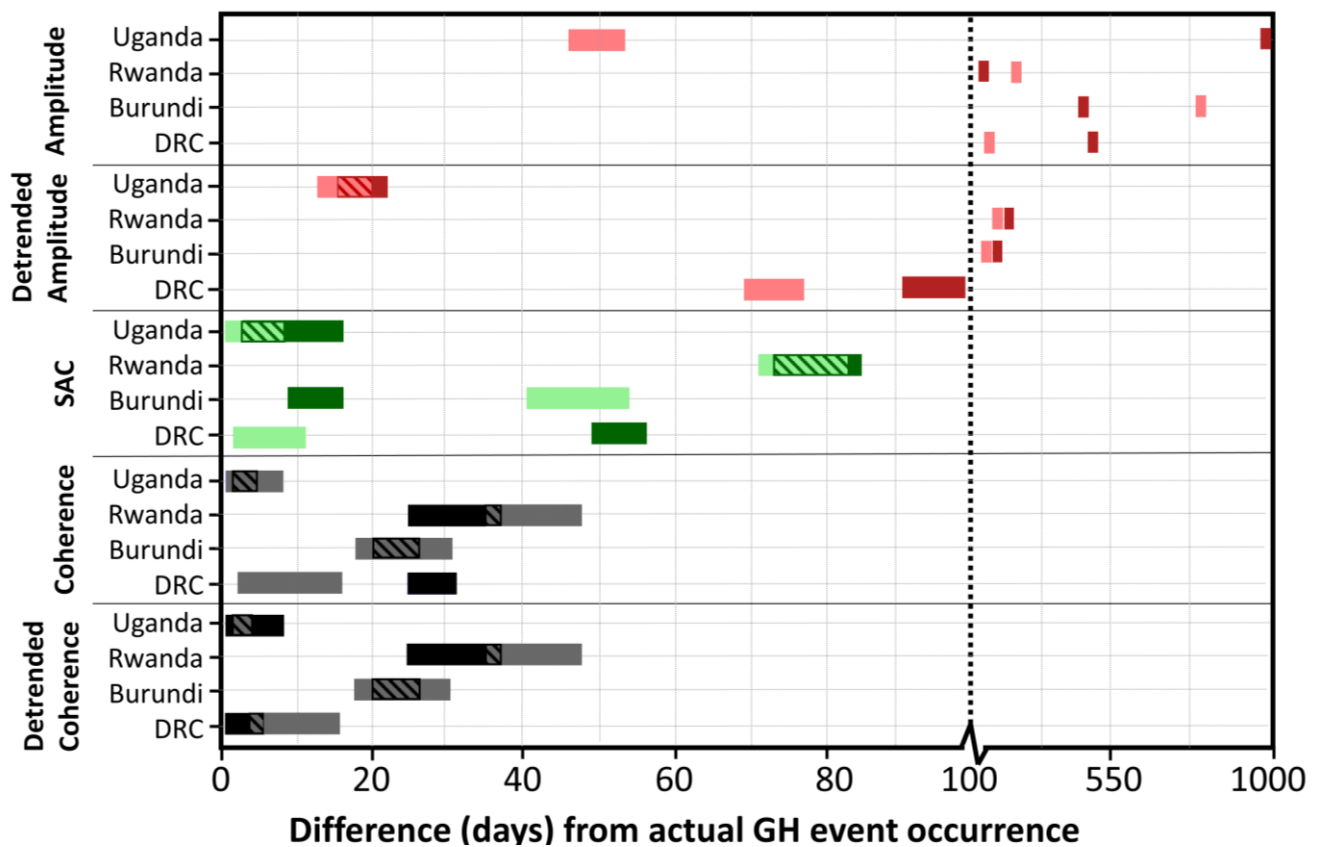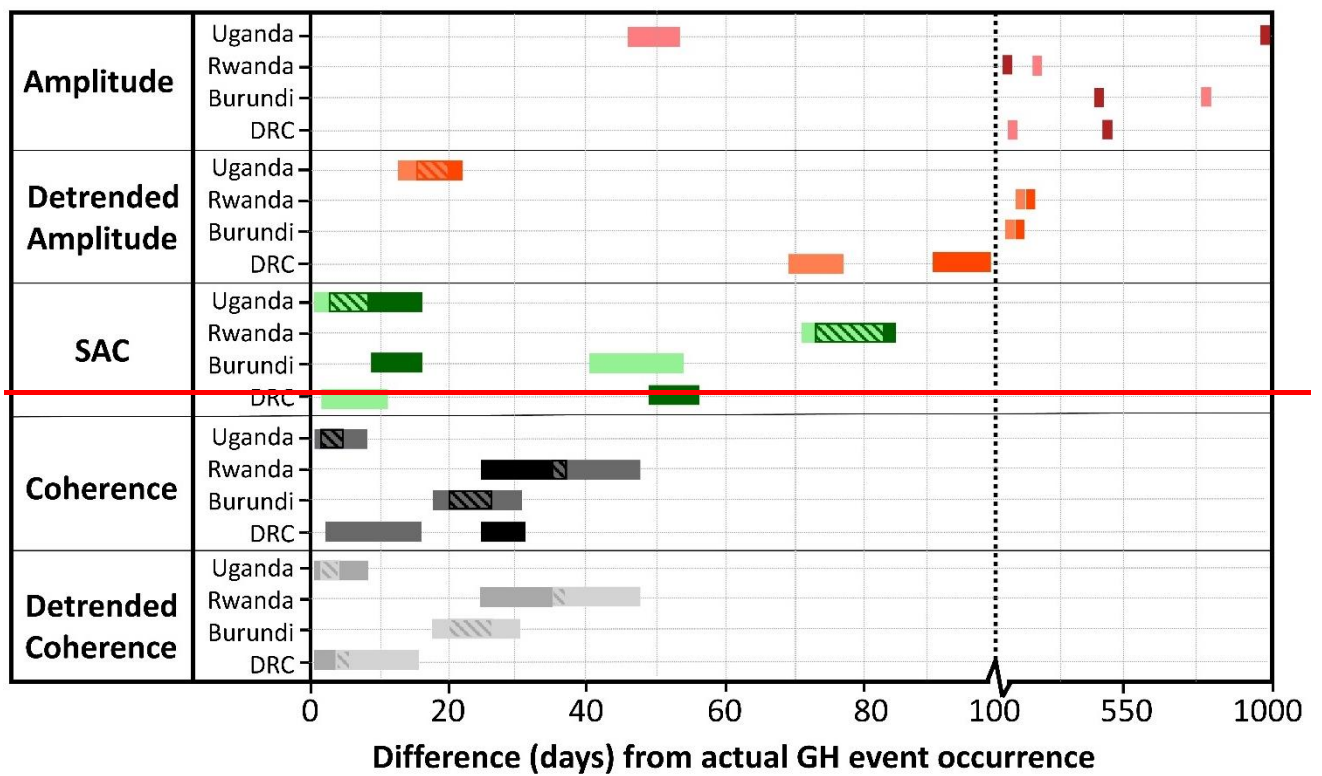
548 *Figure 7.: Estimated GH event timing using the complete GH event scale (workflow 1) for amplitude,*

549 *detrended amplitude (red), SAC (green), coherence and detrended coherence (black). The darker*

550 *colored bar representing the ascending track results. The lighter colored bar representing the*

descending track results. .The length of bars represent the uncertainty in timing (see section 3.3). Per GH event two bars indicate the estimated timing. The darker color bar visualizes the timing range estimated from ascending track imagery and the lighter color bar visualizes the timing range estimated from descending track imagery. The color dashedDashed lines on the bars (▨) represents the overlap between the ascending and descending track timing estimationsresults.
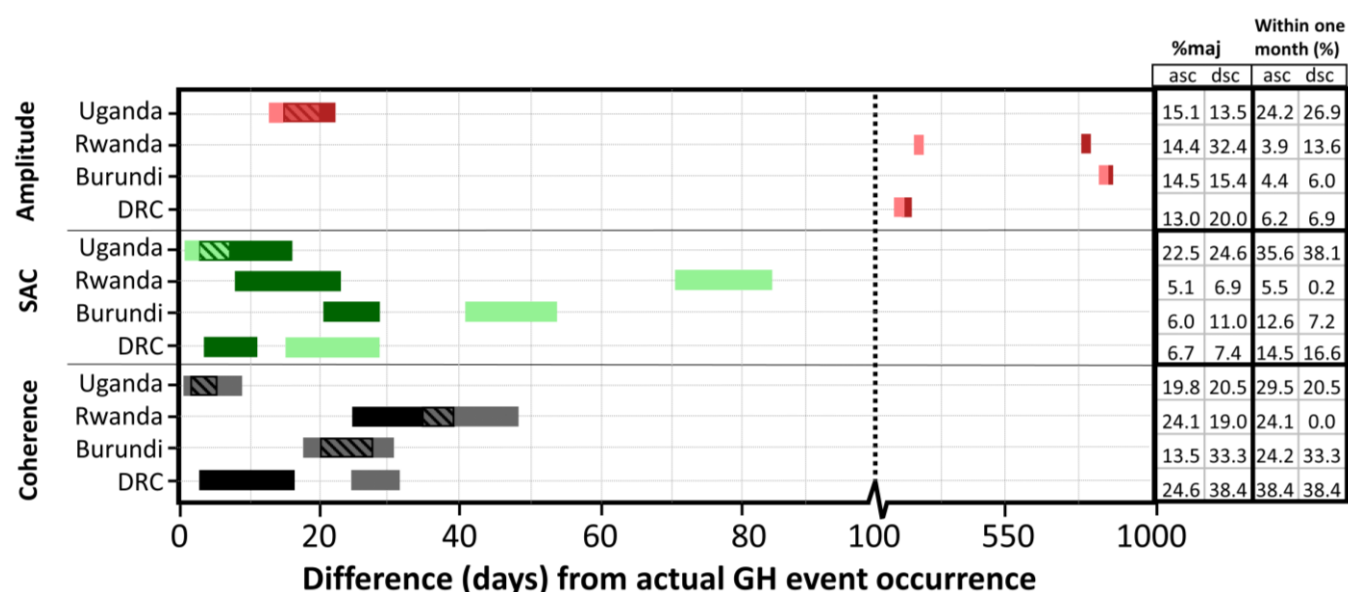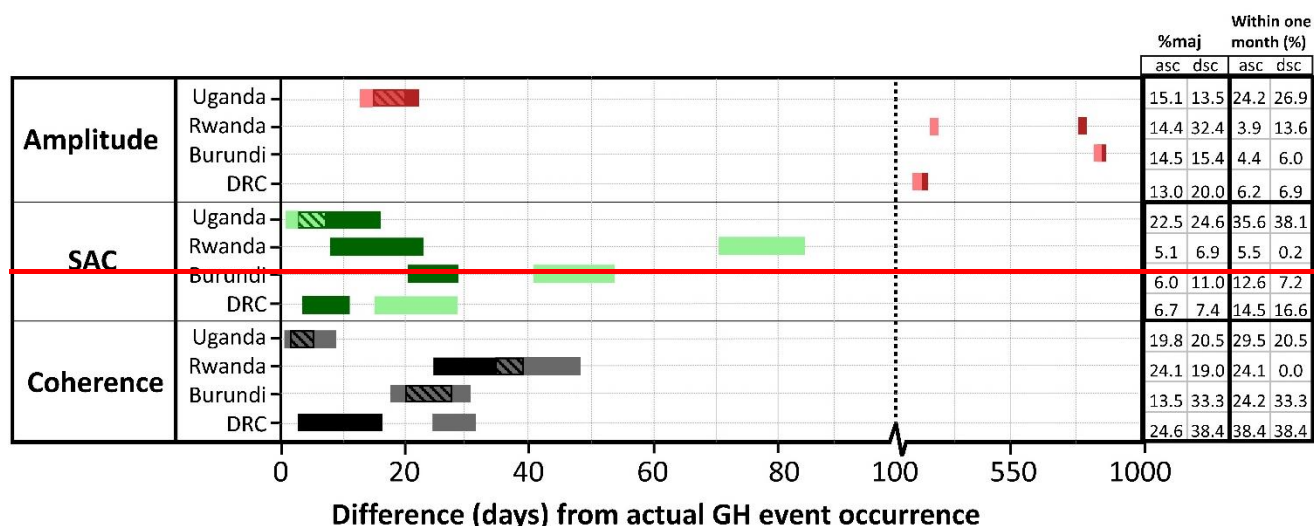
Figure 8: Estimated timing from the individual GH *feature scale (workflow 2) for amplitude, detrended amplitude (red), SAC (green), coherence and detrended coherence (black). The darker colored bar representing the ascending track results.* The *length of* bars represent the uncertainty in timing *(see section 3.3).* ~~Per GH event two bars indicate the estimated timing. The darker color bar visualizes the timing range estimated from ascending track imagery and the lighter color bar visualizes the timing range estimated from descending track imagery.~~ *Dashed lines on the bars represent the overlap between the ascending and descending track results.* ~~The color dashed bar (▨) represents the overlap between ascending and descending track timing estimations.~~ In the %maj column we present the percentage of individual GH features over the total amount of individual GH features that were included in the majority vote separated for the ascending (asc) and descending (dsc) track. In the 'within one month' column we present the percentage of individual GH features over the total amount of individual GH features that estimated a date within one month of the actual event occurrence.

4.3. ~~Time series~~Sensitivity analysis with respect to landscape characteristics

571 GH size seems to have a clear influence on time estimation accuracy. Specifically, the SAC and coherence

572 show a clear increase in percentages of estimated timing within one month of the GH event occurrence

573 with increasing GH size (fig. 9 a-f). R^2 values show a relatively reliable fit for both SAC and coherence.

574 Amplitude shows a slight increasing trend, but associated R^2 values are ~~non-reliablenon~~ non-significant~~i~~

575 .

576 Slope trend lines (fig. 9 g-l) show in general little to no inclination and R^2 -values are ~~non~~ non-

577 significant~~insignificant~~, except for the coherence ascending track. Here, a clear increase in slope angle

578 becomes visible with a comparatively higher R^2 (although clearly less ~~reliable~~ significant than R^2 from

579 the ~~area~~ GH size analysis).

580 To assess the general influence of land cover on the ability to estimate GH event timing we combined

581 both the ascending and descending track results for all four GH events in each boxplot (fig. 9 m-o).

582 Each boxplot therefore contains a total of eight data ~~sources~~ points per land cover type. The major land

583 cover classes within the GH events were tree covered area, grassland, and cropland (Fig 4d). Median

584 percentage values range around 9-10 % for amplitude, 11-16 % for SAC, and 27-34 % for coherence.

585 Although median values within the grassland land cover type seem to be systematically higher among

586 the three~~3~~ data products (amplitude, SAC, and coherence), differences with other land covers are quite

587 small. No specific land cover shows a significant ~~advantage~~better performance.

588 To assess the influence of the slope orientation, we derive the difference between ascending and

589 descending track percentages per bin and determine which track shows better performance (fig. 9p-s).

590 At the results for the Rwanda GH event (fig. 9q) we see for SAC and coherence an all-round favorability

591 for the ascending track, that can be explained by the fact that, like the results in figure 8, the Rwanda

592 GH event had almost no estimations within one month of the GH event occurrence for the descending

593 track. The results presented for Uganda, Burundi and DRC GH events (fig. 9p,r,s) show a general

594 favorability of the ascending track for individual GH features that have an aspect of approximately 45-

595 180°, whereas a general favorability of the descending track for individual GH features that have an

596 aspect of approximately 225-360°. In contrast to this general trend, the opposite seems to be visible

597 for the Uganda GH event coherence.

598
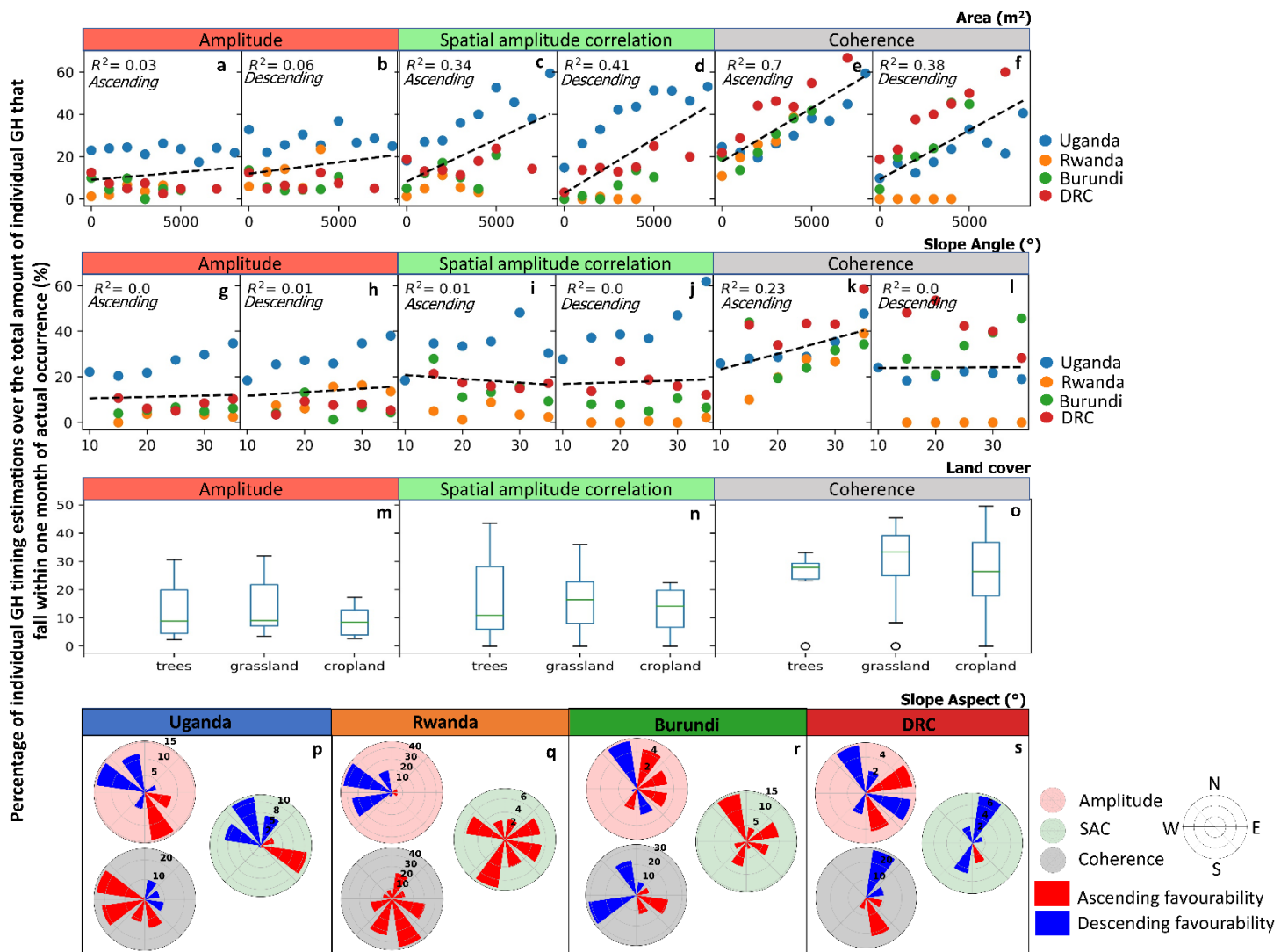
Figure 9. – Timing estimation performance over changing individual GH feature area (a-f), slope angle (g-l), land cover (m-o) and slope aspect (p-s). The y-axis displays the percentage of individual GH features that estimated a timing that falls within one month of the actual GH event occurrence over the total amount of individual GH features per GH event. Bin sizes: area=1000m, slope angle=5°, slope aspect=45°. Area (a-f) and slope angle (g-l) plots are separated per track, and the colors indicate the different GH events. The black dashed lines present the linear trend lines fitted to the data (a-l) for which the associated R^2 values are included. Land cover (m-o): boxplots give lower and upper quartiles and median. The whiskers of each box represent 1.5 times the interquartile range. Outliers beyond whiskers are shown as dots. Slope aspect (p-s): the polar plots present the favorability of the ascending (ASC) or descending (DSC) track per slope aspect (see section 4.3). The color of the polar plot background indicates the SAR data product.

5 Discussion

In this study we present a regionally applicable methodology to automatically determine GH event timing using S1 SAR data. Our study improves on the recent advances in GH event timing estimation research as: (1) we are one of the firsts to use amplitude, SAC and coherence time series in a systematic manner to detect the timing of GH events (Mondini et al., 2021), (2) we defined a methodology where no prior knowledge of the GH event timing is required, (3) we applied our methodology on contrasting landscapes and (4) we combined, for the first time, landslides and flash floods in a single detection approach. Here we discuss our insights, results considering recent developments, and the potential improvements and future perspectives of our ~~new method~~methodology.

5.1. Insights in geomorphic hazard~~GH~~ event timing estimation from SAR

5.1.1 Geomorphic hazard~~GH~~ event timing estimation

The use of amplitude or detrended amplitude time series in our methodology does not prove to be an effective approach to accurately determine the timing of GH events since it gives an estimation accuracy of 13 to 1000 days with the actual time occurrence of the events. A clear increase in accuracy is obtained from SAC with an accuracy of 1 to 85 day. However, the most accurate results are achieved with coherence and detrended coherence with a 1 to a 47 day accuracy.

GH event timing accuracies are higher for GH events that occurred in remote areas with low amounts of cultivation and human influence (highest accuracies for Uganda GH event, lowest for Rwanda GH event). The magnitude of the seasonal vegetation oscillations, which shows connectivity with the precipitation patterns (fig. 6), varies significantly with changing landscapes and results in profound seasonal cyclicity in both the amplitude and coherence timeseries. Although the coherence is additionally influenced by atmospheric effects (Rocca et al., 2000), the influence of both the vegetation and atmosphere on the coherence does not obscure the GH event induced change within the time series. Notably, after detrending, the effects of both seem to be almost negligible. Denser and taller vegetation, result in lower seasonal cyclicity within the amplitude and coherence time series. S1 operates in C-band frequency, meaning that the emitted signal penetrates the canopy layer and subsequently bounces on the branches, and leaves underneath (Dzurisin, 2006). A reduction in vegetation after a seasonal dry period within sparsely vegetated areas, i.e., the grass- and croplands in the DRC GH event, will likely expose the soil underneath and have a pronounced influence on the backscattering signal given the difference in backscattering properties of vegetation and soil (Strozzi et al., 2000, Weydahl, 2001, Colsesanti & Wasowski, 2006, Tessari et al., 2017). In contrast, a seasonal dry period in a dense forest, (i.e., Uganda GH event) would affect the density of the canopy cover. However due to the height and close vicinity of the vegetation to each other a dry period does not necessarily lead to more soil exposure. This ~~is corroborated~~is corroborated ~~by the~~by the fact that the NDVI does not change much for the Uganda GH event, despite the seasonal patterns in precipitation (fig. 6). The regions that are covered with the denser and most uniform vegetation are commonly environments with the lowest chance of getting timing information from other sources (media, citizen-observer networks) as compared to GH events in more inhabited landscapes (Jacobs et al., 2019, Monsieurs et al., 2019,).

648 The complex reaction of the SAR signal to soil moisture and roughness change can causes both an in-
649 and decrease of the amplitude at the same GH event location (Mondini et al., 2021, Burrows et al.,
650 2022). Next to the seasonal influence (fig. 6), this can also be a potential reason why no significant
651 changes at the timing of the GH event are distinguished for all GH events. The inter-pixel variation
652 captured in SAC proves to be a good tool to account for both this potential in- and decrease and any
653 seasonal variation in amplitude values at the location of the GH event and increased timing estimation
654 accuracy.

655 The pre-event, co-event, and post-event coherence values of our four GH events correspond with the
656 study of Tzouvaras et al. (2020), where a distinct difference in pre- (low) and post- (high) GH event
657 coherence values is observed at the location of a landslide occurrence. We observe the same patterns
658 with the GH events that contain flash floods, likely because a clear landscape change is observed after
659 the occurrence of the (often sediment-rich) flash floods (fig. 1). The co-event coherence drop as
660 observed by Tzouvaras et al. (2020) and Burrows et al. (2019) at the location of a landslide occurrence
661 does not prove to be significant enough to be able to determine GH event timing. This is most likely
662 attributed to the fact that the GH events occurred in low-coherence (vegetated) areas (Weydahl 2001,
663 Tessari et al., 2017).

5.1.2 Geomorphic hazardGH event distribution

665 An increase in GH area improves the accuracy of timing detection, which can likely be related to the
666 increased number of pixels fully covering the GH feature relative to the fuzzy edge pixels (e.g. Foody
667 and Mathur, 2006, Deijns et al., 2020, Zhong et al., 2021).

668 Generally, accuracy is not correlated with slope angle (fig. 9). However, an increase in accuracy with
669 increasing slope with a relative low reliability is observed for coherence. Nevertheless, this trend must
670 be considered with a certain caution: (1) the trend is dependent on the quality of terrain correction
671 during the pre-processing step (section 3.1), which should make SAR values independent of slope angle
672 (Small, 2011), (2) a changing slope angle could influence the GH size (Chen et al., 2016), (3) we take
673 the average slope angle per GH. Elongated GH features (mainly the flash flood features in the GH
674 inventories) will have an average slope angle that is not representative for every part of the GH.

675 Although a clear difference can be observed in time series response to GH events located in different
676 landscapes (fig. 6), the comparison with the land cover does not allow to find a clear relationship with
677 the type of vegetation (fig. 9). Since the land cover distribution is not equal amongst GH events (fig.
678 5), the results are, for some GH events, based on a low amount of individual GH features. The, which
679 might not be representative enough for a general trends could therefore also be influenced by additional
680 underlying trends such as GH size and GH slope angle. The observed large variation in values per box
681 plot (fig. 9m-o) might be an indication of this.

682 By using the right-looking S1 satellite data, foreshortening, and layover effects should be limited with
683 descending track acquisitions for GH exposed towards the west (180-360°) and with ascending track

acquisitions for GH exposed towards the east (0-180°). The shadow affects in the opposite direction and is dependent on the slope of the terrain (Bamler, 2000). We see that, generally, the individual GH-features on the descending slope tend to have a higher timing estimation accuracy for the west facing slopes and the individual GH features on de ascending track for the east facing slopes, which is as expected. However, there remains variability in the result, for example, an opposite pattern is visible for Uganda GH event with the coherence and a partial favorability for the descending track acquisition on east facing slopes is visible for the DRC GH event. Future research on the detailed effect of changing GH feature aspects on the ascending and descending SAR time series can provide additional valuable information in this context.

Our derived trends are established from GH events with each 318 to 1063 individual GH features and provide a good indication of the SAR response to changing landscape parameters. It remains interesting to see if these trends sustain with the addition of more GH events from different landscapes.

5.2. Result considering recent developments in SAR timing detection

Our results are somewhat in contrast with Burrows et al., (2022), who argue that coherence is less performant than amplitude for GH event timing. ~~Burrows et al. (2022) used a method similar to our timing workflow 2, where they estimated timing from individual landslides and chose the majority to represent the timing.~~ Using amplitude data, they were able to estimate the timing of ~ 3~~2~~0% of landslides per inventory with ~~an accuracy of 6-12 days with~~an accuracy of ~80% ~~confidence~~and an average precision of 12 days. Whereas by using coherence (60x60m resolution) they acquired much ~~lower~~ less ~~confidence~~ accurate results ~~values~~ (24-47% correctly estimated). Their study, however, differs in several aspects from our analysis:

1. Burrows et al., (2022) applied their method with a pre-defined notion of GH event timing, i.e. known year and season. For our GH events, we see distinct seasonal dynamics mainly within the amplitude time series. Zooming in on a specific time frame (3 months before and 3 months after the GH event occurrence like Burrows et al., (2022)) reduces the overall seasonal dynamics, which could be the cause of a wrongly identified GH event change. Reducing this time window will potentially ~~This~~ improve~~s~~ the detectability of the GH event within the time series ~~and thus the resulting accuracies~~. However, our methodology is ~~also~~ intended to be applicable in areas such as the western branch of the East African Rift, an area ~~that are~~ characterized by data scarcity (Dewitte et al., 2021). In areas like these, information on the temporal distribution of GH events may not always be available. We therefore defined a methodology that requires no knowledge on GH event timing before application, which is an advantage if no GH event timing is present, however, this increases the chance of any seasonal influence visible within the time series.

2. They applied their method on landslides only. In our case, the addition of flash floods to the inventories introduces different types of contrasting GH shapes, slopes and land cover (flash floods tend to be elongated, occur in the valleys with shallower terrain, whereas landslides occurred mainly on the steeper hillslopes) that can influence the SAR time series, specifically if the flash flood enters

721   urbanized area (such as in the DRC GH event) or run through a seasonally dynamic channel with

722   seasonally changing soil moisture levels influencing the SAR signal (Ulaby et al., 1996, Scott et al.,

723   2017).

724 3. Their used landslide inventories (from Roback et al., 2018 and ~~,~~ Emberson et al., 2022) ~~suggest~~

725   ~~that they developed their method on landslides in comparatively more ideal homogenous landscape~~

726   ~~conditions, where the landslides generally occurred in denser vegetated areas with less cultivated~~

727   ~~area. This is corroborated by their high pre-event NDVI values (peak of distribution between 0.7-~~

728   ~~0.8).~~are located in densely vegetated areas (NDVI between 0.6 and 0.8). ~~In the three areas they~~

729   ~~studied, Zimbabwe, located in a semi-arid climate region (Roback et al., 2018) is the region where~~

730   ~~the landscape is the least homogenous and the closest to what we study. In Zimbabwe however,~~

731   ~~landslides generally still occur in vegetated areas (including grassland, forests) without significant~~

732   ~~agricultural practices, which is in contrast with the Rwanda and DRC GH events in our study that~~

733   ~~have a large portion of the GH within crop- and grassland (fig. 5).~~ In agreement with Burrows et al.

734   (2022) our results show that the Uganda GH event, where most of the landscape consists of dense

735   vegetation (i.e., the highest NDVI values), ~~show~~ estimated GH event timing accuracies ~~that~~ are the

736   highest among all GH events, obtaining a 1-2 images difference from the actual GH event occurrence

737   for SAC (1-16 days) and (detrended) coherence (1-8 days). Although amplitude is overall less

738   performant for the Uganda GH event, we still achieve an accuracy off 13-22 days for the detrended

739   amplitude.

740 4. We do not threshold on individual GH area. Specifically, the Rwanda GH event contains a GH event

741   size distribution that includes many small individual GH features below th~~e~~~~is~~ threshold used in

742   Burrows et al. (2022) ~~(fig. 5).~~ Together with the complexity and large fraction of cultivation of the

743   landscape this clearly results in reduced estimation accuracies.

744 ~~5. To improve timing accuracy, t~~They removed landslide timing estimations ~~that did not pass a~~

745   ~~threshold based on the relative~~using the magnitude ~~of of the~~ change caused by the landslide with~~in~~

746   the SAR time series~~, induced by the landslides~~ which allowed them to improve the estimation

747   accuracy.

748 5.

5.3 Improvements and perspectives

750 The current methodology successfully allows to analyze GH event timing from SAR, but several

751 improvements can be considered in future research.

5.3.1 Improvements

753 1. In the current methodology we do not detrend individual GH feature time series (see section 3.3).

754   Because detrending does increase timing accuracy within our study, further research on accurate

755   detrending of individual GH time series can potentially greatly benefit timing estimation accuracy.

756 ~~2.~~ We use ~~one point~~one change detection algorithm (ruptures: Truong et al., 2020) ~~to find changes~~

757   ~~related to the GH event occurrence within the time series~~to estimate GH event timing. Comparing

multiple change detection algorithms (e.g.~~, the ones used by~~Deijns et al., 2020, Burrows et al.~~,~~ ~~(~~2022~~)~~), could potentially benefit GH event timing estimation accuracy. ~~Additionally, within our timing workflow 2, we do not incorporate any methodology to filter out any low accuracy timing estimations, such as in Burrows et al., 2022. However, since we do not apply the methodology with a pre-defined notion of time, our time series are prone to seasonal dynamics (fig. 6) and the applicability of such an implementation remains to be investigated.~~

2.

3. The quality of the amplitude and coherence imagery is dependent on the quality of the pre-processing applied with the MasTer tool (Derauw et al., 2020, d'Oreye et al., 2021) and how it deals with the different steps such as co-registration, radiometric terrain correction and geocoding. Quality of the imagery in its turn is also dependent on, among others, the multi-look factor (amplitude), the interferometric multi-look factor and the maximum temporal and perpendicular baselines (coherence). In addition, different polarizations may yield different results (Shibayama et al., 2015, Psomiadis, 2016, Park & Lee, 2019) and the use of a different polarization can potentially improve event detectability within the time series. Improvements within the SAR imagery might be achieved by tweaking and closely investigating different pre-processing steps to achieve better image quality.

4. The SAC result depends on the ability to find the best reference image (~~s~~Section 3.2). ~~Additional efforts can be made to better find the SAC time series that shows the most significant change related to the GH event occurrence. For example, a preliminary filtering of very noisy SAC time series (before applying our developed method using the ECDF's) can potentially benefit the ability to acquire the best reference image.

5.3.2 Perspectives

1. We have studied, for the first time in a GH event timing detection approach, both landslides and flash floods in a combined methodology. Since these GH often co-occur and interact (Marengo & Alves, 2012, Jacobs et al., 2016a, Rengers et al., 2016) they should be analyzed in a multi-hazard approach. Our method~~ology~~ can be well applied within ~~a multi-hazard methodology~~such an approach. For example, multi-hazard inventories can serve as ~~an~~ input for our methodology if there is a need to improve ~~event~~ their timing accuracy. ~~Regional results~~Results can subsequently be used in hazard assessment, early warning, and disaster risk reduction strategies.

2. Our study shows that there is a clear advantage to analyzing different S1 SAR data products when estimating GH event timing. The fact that Burrows et al. (2022) shows better results for amplitude compared to coherence data is in contrast with our results but reinforces the idea of investigating both data products when applying the method~~ology~~ to new regions.

3. ~~Regarding transferability of our developed method.~~ Given the clear influence of landscape and climate as controlling factors for SAR time series behavior (~~elaborated in~~ section 2.3), we aimed to develop our method~~ology~~ within a variety of contrasting landscapes and contrasting vegetation dynamics. This offers perspectives for transferability. We show that ~~s~~Slope angle does not seem to influence accuracy (fig. 9). Based on landscape characteristics, t~~T~~ransferability to other regions

seems therefore likely to acquire good results, specifically for the SAC, coherence and detrended coherence time series as they do seem less influenced by seasonal dynamics than the amplitude and detrended amplitude time series (fig 6.). However, climate drivers could also potentially play a role. ~~The precipitation regime within our study area is quite similar for the four studied GH events (Nicholson 2017, Monsieurs et al., 2018a).~~ For example, Since soil moisture and wetness have an influence on amplitude and coherence time series (Ulaby et al., 1996, Srivastava et al., 2006, Brancato et al., 2017, Scott et al., 2017), contrasting precipitation regimes within other regions could potentially influence the response of the SAR time series and the estimated GH event timing accuracy. Examples of contrasting precipitation regimes are: (1) a lower amount of precipitation in more arid regions, or lower/higher amounts in other tropical regions (Fick and Hijmans, 2017); ~~-~~(2) a change in precipitation seasonal variability due to spatially different oscillation of the ITCZ (Nicholson et al., 2017, Dewitte et al., 2022); ~~-~~ (3) the effect of local topography and the presence of lakes on the local precipitation patterns (~~e.g.~~e.g. Thiery et al., 2015; 2016; 2017, Monsieurs et al., 2018b). The influences of these contrasting precipitation regimes on SAR-based GH timing ~~detection~~detection, however, remains to be investigated. Additionally, in its current form, the methodology does not account for the GH events that occur within a time span that is longer than the acquisition time (> 6-12 days) of S1 images (i.e. multi-temporal GH events). In that case one would require a time window of occurrence, rather than a specific date. The methodology can be adapted to allow it to derive a time window of GH occurrence. This could mainly be done following ~~timing workflow~~ the ~~1 (the~~ GH event scale~~)~~, where~~.~~ ~~t~~The start and the end date of the GH event inducing change within the SAR time series (applicable for all data products) should be indicative of the time window of GH event occurrence. However, this remains to be investigated.

4. The open-access S1 satellite with its high resolution, high repeat time and global coverage proves to be an excellent data product for estimating GH event timing and allows for our developed methodology to be applied on every region of the world. The use of our methodology with different satellite products (e.g. COSMO-SkyMed, upcoming NISAR satellite) is not straightforward. Different available SAR satellite products operate in different bands with their own characteristics ~~-~~(e.g.~~,~~ X-band for COSMO-Sky~~M~~med (Covello et al., 2010) and ~~-~~L-band for NISAR (NISAR, 2018)), that will likely have~~.~~ implications on the ability for accurate GH event timing estimation. For example, the varying vegetation penetration depths associated with different SAR bands (Dzurisin, 2006) will likely have an influence on the impact of seasonal vegetation dynamics on the SAR time series as observed for our GH events (fig. 6). ~~, which have varying vegetation penetration depths (Dzurisin, 2006). The effect related to varying vegetation penetration depthsSAR products remains to be investigated~~

5. The methodology can benefit (in terms of data availability, scalability, and processing time) from implementation on a cloud computing service. ~~However, these~~ ~~c~~Cloud computing platforms such as GEE only provide pre-processed amplitude imagery (i.e. amplitude ground range detected imagery). As such, they ~~This will~~ allow for the applicability of our methodology using the amplitude, detrended amplitude and SAC data products. ~~However,~~T~~to our knowledge, so far no cloud

836 computing platform offer ~~, but there is so far no~~the possibility for processing and using coherence

837 data. Additionally, the use of pre-processed amplitude imagery restrains us from manual input

838 during the pre-processing step (as the MasTer Toolbox allows).

839 6. The methodology can potentially be combined with optical data (e.g. Deijns et al., 2020) that could

840 serve as additional data to help narrow down the time window and filter out any non-sense timing

841 estimations.

6. Conclusion

843 We established a ~~new~~ regionally applicable methodology to automatically determine GH event timing

844 from SAR images, that can be applied without prior knowledge of the GH event. ~~And~~W~~we~~ we successfully

845 assessed the use of multiple SAR derived data products in their ability to accurately detect GH event

846 timing ~~for~~in contrasting ~~types of landscape~~landscapes. ~~Our methodology method is original as it is the~~

847 ~~first time that landslides and flash floods are studied together. By~~ We show~~ing~~ that ~~these two~~

848 ~~processes~~landslides and flash floods can be detected and ~~therefore~~ studied together~~,~~, hence we open

849 new perspectives in the study of multi-hazards, that can subsequently ~~which can~~ aid in hazard

850 assessment, early warning, and disaster risk reduction strategies. Our methodology has the potential to

851 be combined with existing spatial detection methods to support inventory creation and boost GH event

852 research in remote inaccessible areas such as the African cloud-covered tropics.

853 From a data processing point of view, the methodology is established around an unprecedented analysis

854 of various SAR products coming from Sentinel-1 (S1) images. We show that there is a need to investigate

855 different SAR data products when estimating GH event timing (amplitude, spatial amplitude correlation,

856 and coherence) since the signal response can be different and sometimes contradictory when looking

857 at one single event. The implementation of our methodology ~~method~~ on a cloud computing platform

858 can be beneficial in terms of scalability, data availability and processing time. However, the main

859 limitations in this context are: (1) no control in pre-processing of S1 imagery and, (2) S1 coherence

860 data is so far not available within these platforms.

861 With a focus on four events containing a total of about 2500 landslides and flash flood features in

862 contrasting landscapes, we propose a methodology ~~method~~ that is adapted to be applied to other

863 regions. Here, we focused on tropical environments where climate conditions and land use dynamics

864 are rather specific. However, we believe that the complexity of these landscapes is an added value for

865 the transferability of the methodology. Additionally, the use of the globally available open access S1

866 satellite data allows our methodology ~~method~~ to be applied on every region of the World.

Acknowledgement

868 This study was supported by the Belgium Science Policy (BELSPO) through the PAStECA project

869 (BR/165/A3/PASTECA) entitled "Historical Aerial Photographs and Archives to Assess Environmental

870 Changes in Central Africa" (http://pasteca.africamuseum.be/, last access 09 June 2022). The

871   compilation of the inventory data benefited from field-based insight and discussion with Arthur Depicker,

872   Josué Mugisho Bachinyaga, John Sekajugo and Judith Uwihirwe. PlanetScope data provided by the

873   European Space Agency.

Code and data availability

Sentinel-1 and Sentinel-2 data are provided open-access by the European Space Agency. Landsat 8 data are provided open access by the U.S. Geological Survey. The Python scripts for the GH event timing estimation, sensitivity analysis, and precipitation analysis and the Google Earth Engine code for vegetation analysis can be accessed at: ZENODO LINK will be provided once the manuscript is accepted for publication. The four GH inventories can be downloaded at: ZENODO LINK

Author contribution

AAJD, OD, FK and WT conceived the study. AAJD compiled the landslide and flash flood inventory with the support of OD. AAJD processed and analyzed the data. OD conducted field work for the validation of the inventory. AAJD wrote the original draft of the manuscript, with key initial input from OD and FK. NO trained AAJD in SAR image pre-processing. All the authors contributed to reviewing and editing the manuscript. OD obtained funding for this work.

Competing interests.

The authors declare no conflict of interest.

References

Aimaiti, Y., Liu, W., Yamazaki, F. and Maruyama, Y.: Earthquake-induced landslide mapping for the 2018 Hokkaido Eastern Iburi earthquake using PALSAR-2 data. Remote Sens., 11(20i), 2351, https://doi.org/10.3390/rs11202351, 2019

Ali, K., Bajracharyar, R.M. and Raut, N.: Advances and challenges in flash flood risk assessment: A review. J. Geogr. Nat. Disast. 2017, 7(2), 1-6, https://doi.org/10.4172/2167-0587.1000195, 2017

Bai, J.: Estimating multiple breaks one at a time. Econ. Theory, 13, 315-352, https://doi.org/10.1017/S0266466600005831, 1997

Balzter, H.: Forest mapping and monitoring with interferometric synthetic aperture radar (InSAR). Prog. Phys. Geogr., 25(2), 159-177, https://doi.org/10.1177/030913330102500201, 2001

Bamler, R.: Principles of synthetic aperture radar. Surv. Geophys., 21(2), 147-157, https://doi.org/10.1023/A:1006790026612, 2000

Barrett, B., Whelan, P. and Dwyer, E.: The use of C-and L-band repeat-pass interferometric SAR coherence for soil moisture change detection in vegetated areas. Open Remote Sens. J., 5, 37-53, https://doi.org/10.2174/1875413901205010037, 2012

Behling, R., Roessner, S., Kaufmann, H. and Kleinschmit, B.: Automated spatiotemporal landslide mapping over large areas using rapideye time series data. Remote Sens., 6(9), 8026-8055. https://doi.org/10.3390/rs6098026, 2014

Behling, R., Roessner, S., Golovko, D. and Kleinschmit, B.: Derivation of long-term spatiotemporal landslide activity—A multi-sensor time series approach. Remote Sens. Environ., 186, 88-104, https://doi.org/10.1016/j.rse.2016.07.017, 2016

Bonfils, S.: Trend analysis of the mean annual temperature in Rwanda during the last fifty two years. J. Environ. Prot. 3(2), 20077, https://doi.org/10.4236/jep.2012.36065, 2012.

Bradshaw, C.J. a., Sodhi, N.S., Peh, K.S.H., Brook, B.W.: Global evidence that deforestation amplifies flood risk and severity in the developing world. Glob. Chang. Biol. 13, 2379–2395, https://doi.org/10.1111/j.1365-2486.2007.01446.x, 2007

Brancato, V., Liebisch, F. and Hajnsek, I.: Impact of plant surface moisture on differential interferometric observables: A controlled electromagnetic experiment.. IEEE Trans. Geosci. Remote Sens., 55(7), 3949-3964, https://doi.org/10.1109/TGRS.2017.2684814, 2017

Burrows, K., Walters, R.J., Milledge, D., Spaans, K. and Densmore, A.L.: A new method for large-scale landslide classification from satellite radar. Remote Sens., 11(3), 237, https://doi.org/10.3390/rs11030237, 2019

Burrows, K., Walters, R. J., Milledge, D., and Densmore, A. L.: A systematic exploration of satellite radar coherence methods for rapid landslide detection, Nat. Hazards Earth Syst. Sci., 20, 3197–3214, https://doi.org/10.5194/nhess-20-3197-2020, 2020.

Burrows, K., Milledge, D., Walters, R. J., and Bellugi, D.: Integrating empirical models and satellite radar can improve landslide detection for emergency response, Nat. Hazards Earth Syst. Sci., 21, 2993–3014, https://doi.org/10.5194/nhess-21-2993-2021, 2021.

Burrows, K., Marc, O., and Remy, D.: Establishing the timings of individual rainfall-triggered landslides using Sentinel-1 satellite radar data, Nat. Hazards Earth Syst. Sci. Discuss. [preprint], https://doi.org/10.5194/nhess-2022-21, in review, 2022.

Burrows, K., Marc, O., and Remy, D.: Using Sentinel-1 radar amplitude time series to constrain the timings of individual landslides: a step towards understanding the controls on monsoon-triggered landsliding, Nat. Hazards Earth Syst. Sci., 22, 2637–2653, https://doi.org/10.5194/nhess-22-2637-2022, 2022

Casagli, N., Frodella, W., Morelli, S., Tofani, V., Ciampalini, A., Intrieri, E., Raspini, F., Rossi, G., Tanteri, L., Lu, P.: Spaceborne, UAV and ground-based remote sensing techniques for landslide mapping, monitoring and early warning. Geoenviron. Disasters 4, 9. https://doi.org/10.1186/s40677-017-0073-1, 2017

Chen, X.L., Liu, C.G., Chang, Z.F. and Zhou, Q.: The relationship between the slope angle and the landslide size derived from limit equilibrium simulations. Geomorphology, 253, 547-550, https://doi.org/10.1016/j.geomorph.2015.01.036, 2016

940 Colesanti, C. and Wasowski, J.: Investigating landslides with space-borne Synthetic Aperture Radar
941 (SAR) interferometry. Eng. Geol., 88(3-4), 173-199, https://doi.org/10.1016/j.enggeo.2006.09.013,
942 2006

943 Covello, F., Battazza, F., Coletta, A., Lopinto, E., Fiorentino, C., Pietranera, L., Valentini, G. and Zoffoli,
944 S.: COSMO-SkyMed an existing opportunity for observing the Earth. J. Geodyn. 49, 171-180,
945 https://doi.org/10.1016/j.jog.2010.01.001, 2010

946 Deijns, A.A.J., Bevington, A.R., van Zadelhoff, F., de Jong, S.M., Geertsema, M. and McDougall, S.:
947 Semi-automated detection of landslide timing using harmonic modelling of satellite imagery,
948 Buckinghorse River, Canada. Int. J. Appl. Earth Obs. Geoinf, 84, 101943,
949 https://doi.org/10.1016/j.jag.2019.101943, 2020

950 Depicker, A., Jacobs, L., Mboga, N., Smets, B., Van Rompaey, A., Lennert, M., Wolff, E., Kervyn, F.,
951 Michellier, C., Dewitte, O. and Govers, G.: Historical dynamics of landslide risk from population and
952 forest-cover changes in the Kivu Rift. Nat. Sustain., 4(11), 965-974, https://doi.org/10.1038/s41893-
953 021-00757-9, 2021

954 Derauw, D., Libert, L., Barbier, C., Orban, A., Kervyn, F., Samsonov, S., d'Oreye, N.: The CSL InSAR
955 Suite processor: specificities of a command line InSAR processing software specifically adapted for
956 automated time series processing. ESA Living Planet Symposium 2019, Milano, Italy, 2019. Abstract,
957 13–17., 2019

958 Derauw, D., Jaspard, M., Caselli, A. and Samsonov, S.: Ongoing automated ground deformation
959 monitoring of Domuyo-Laguna del Maule area (Argentina) using Sentinel-1 MSBAS time series:
960 Methodology description and first observations for the period 2015–2020, J. S. Am. Earth Sci., 104,
961 102850, https://doi.org/10.1016/j.jsames.2020.102850, 2020

962 DeVries, B., Huang, C., Armston, J., Huang, W., Jones, J.W. and Lang, M.W.: Rapid and robust
963 monitoring of flood events using Sentinel-1 and Landsat data on the Google Earth Engine. Remote Sens.
964 Environ., 240, 111664, https://doi.org/10.1016/j.rse.2020.111664, 2020

965 Dewitte, O., Dille, A., Depicker, A., Kubwimana, D., Maki Mateso, J.-C.M., Mugaruka Bibentyo, T.M.,
966 Uwihirwe, J. and Monsieurs, E.: Constraining landslide timing in a data-scarce context: from recent to
967 very old processes in the tropical environment of the North Tanganyika-Kivu Rift region. Landslides,
968 18(1), 161-177, https://doi.org/10.1007/s10346-020-01452-0, 2021

969 Dewitte, O., Depicker, A., Moeyersons, J. and Dille, A.: Mass Movements in Tropical Climates.: In:
970 Shroder, J.J.F. (Ed.), Treatise on Geomorphology, vol. 5., Shroder, J.J.F. (Ed.), Elsevier, Academic Press,
971 pp. 338–349Treatise on Geomorphology, 338-349, https://doi.org/10.1016/B978-0-12-818234-
972 5.00118-8, 2022

973 Dobson, M.C. and Ulaby, F.T.: Active microwave soil moisture research. IEEE Trans. Geosci. Remote
974 Sens., 1, 23-36, https://doi.org/10.1109/TGRS.1986.289585, 1986

Dubois, P.C., Van Zyl, J. and Engman, T.: Measuring soil moisture with imaging radars. IEEE Trans. Geosci. Remote Sens., 33(4), 915-926, https://doi.org/10.1109/36.406677, 1995

Dzurisin, D.: Volcano deformation: new geodetic monitoring techniques. Springer, https://doi.org/10.1007/978-3-540-49302-0, 2006

Emberson, R., Kirschbaum, D. and Stanley, T.: New global characterisation of landslide exposure. Nat. Hazards Earth Syst. Sci., 20(12), 3413-3424. https://doi.org/10.5194/nhess-20-3413-2020, 2020

Emberson, R., Kirschbaum, D. B., Amatya, P., Tanyas, H., and Marc, O.: Insights from the topographic characteristics of a large global catalog of rainfall-induced landslide event inventories, Nat. Hazards Earth Syst. Sci., 22, 1129–1149, https://doi.org/10.5194/nhess-22-1129-2022, 2022.

ESA Climate Change Initiative–Land Cover Project 2017. 20 m Resolution, European Space Agency, 2016.

Esposito, G., Marchesini, I., Mondini, A. C., Reichenbach, P., Rossi, M., and Sterlacchini, S.: A spaceborne SAR-based procedure to support the detection of landslides, Nat. Hazards Earth Syst. Sci., 20, 2379–2395, https://doi.org/10.5194/nhess-20-2379-2020, 2020.

Fick, S.E. and Hijmans, R.J.: WorldClim 2: new 1-km spatial resolution climate surfaces for global land areas. Int. J. Climatol., 37(12), 4302-4315, https://doi.org/10.1002/joc.5086, 2017

Foga, S., Scaramuzza, P.L., Guo, S., Zhu, Z., Dilley Jr, R.D., Beckmann, T., Schmidt, G.L., Dwyer, J.L., Hughes, M.J. and Laue, B.: Cloud detection algorithm comparison and validation for operational Landsat data products. Remote Sens. Environ., 194, 379-390, https://doi.org/10.1016/j.rse.2017.03.026, 2017

Foody, G.M. and Mathur, A.: The use of small training sets containing mixed pixels for accurate hard image classification: Training on mixed spectral responses for classification by a SVM. Remote Sens. Environ., 103(2), 179-189, https://doi.org/10.1016/j.rse.2006.04.001, 2006

Froude, M. J. and Petley, D. N.: Global fatal landslide occurrence from 2004 to 2016, Nat. Hazards Earth Syst. Sci., 18, 2161–2181, https://doi.org/10.5194/nhess-18-2161-2018, 2018.

Fryzlewicz, P.: Wild binary segmentation for multiple change-point detection. Ann. Stat., 42(6), 2243-2281, https://doi.org/10.1214/14-AOS1245, 2014

Ge, P., Gokon, H., Meguro, K. and Koshimura, S.: Study on the intensity and coherence information of high-resolution ALOS-2 SAR images for rapid massive landslide mapping at a pixel level. Remote Sens., 11(23), 2808, https://doi.org/10.3390/rs11232808, 2019

Giertz, S., Junge, B. and Diekkrüger, B.: Assessing the effects of land use change on soil physical properties and hydrological processes in the sub-humid tropical environment of West Africa. Phys. Chem. Earth, 30(8-10), 485-496, https://doi.org/10.1016/j.pce.2005.07.003, 2005

Gorelick, N., Hancher, M., Dixon, M., Ilyushchenko, S., Thau, D. and Moore, R.: Google Earth Engine: Planetary-scale geospatial analysis for everyone. Remote Sens. Environ., 202, 18-27, https://doi.org/10.1016/j.rse.2017.06.031, 2017

Guzzetti, F., Peruccacci, S., Rossi, M. and Stark, C.P.: he rainfall intensity–duration control of shallow landslides and debris flows: an update. Landslides 5, 3–17, https://doi.org/10.1007/s10346-007-0112-1, 2008

Guzzetti, F., Mondini, A.C., Cardinali, M., Fiorucci, F., Santangelo, M., Chang, K.-T.: Landslide inventory maps: New tools for an old problem. Earth-Sci. Rev., 112, 42–66, https://doi.org/10.1016/j.earscirev.2012.02.001, 2012

Guzzetti, F., Gariano, S.L., Peruccacci, S., Brunetti, M.T., Marchesini, I., Rossi, M. and Melillo, M.: Geographical landslide early warning systems. Earth-Science Reviews, 200, 102973, https://doi.org/10.1016/j.earscirev.2019.102973, 2020

Hagberg, J.O., Ulander, L.M. and Askne, J.: Repeat-pass SAR interferometry over forested terrain. IEEE Trans. Geosci. Remote Sens., 33(2), 331-340, https://doi.org/10.1109/TGRS.1995.8746014, 1995

Handwerger, A. L., Huang, M.-H., Jones, S. Y., Amatya, P., Kerner, H. R., and Kirschbaum, D. B.: Generating landslide density heatmaps for rapid detection using open-access satellite radar data in Google Earth Engine, Nat. Hazards Earth Syst. Sci., 22, 753–773, https://doi.org/10.5194/nhess-22-753-2022, 2022.

Hanssen, R.F.: Radar interferometry: data interpretation and error analysis, vol 2, Springer, https://doi.org/10.1007/0-306-47633-9, 2001

Heri-Kazi, A. B. and Bielders, C. L.: Cropland characteristics and extent of soil loss by rill and gully erosion in smallholder farms in the KIVU highlands, D.R. Congo, Geoderma Reg., 26, e00404, https://doi.org/10.1016/j.geodrs.2021.e00404, 2021.

Intrieri, E., Raspini, F., Fumagalli, A., Lu, P., Del Conte, S., Farina, P., Allievi, J., Ferretti, A. and Casagli, N. The Maoxian landslide as seen from space: detecting precursors of failure with Sentinel-1 data. Landslides, 15(1), pp.123-133, https://doi.org/10.1007/s10346-017-0915-7, 2018

Jacobs, L., Maes, J., Mertens, K., Sekajugo, J., Thiery, W., Van Lipzig, N., Poesen, J., Kervyn, M., Dewitte, O.: Reconstruction of a flash flood event through a multi-hazard approach: focus on the Rwenzori Mountains, Uganda. Nat. Hazards 84, 851–876, https://doi.org/10.1007/s11069-016-2458-y, 2016a.

Jacobs, L., Dewitte, O., Poesen, J., Delvaux, D., Thiery, W. and Kervyn, M.: The Rwenzori Mountains, a landslide-prone region?. Landslides, 13(3), 519-536. https://doi.org/10.1007/s10346-015-0582-5, 2016b

1042 Jacobs, L., Kabaseke, C., Bwambale, B., Katutu, R., Dewitte, O., Mertens, K., Maes, J. and Kervyn, M.:
1043 The geo-observer network: A proof of concept on participatory sensing of disasters in a remote setting.
1044 Sci. Total Environ., 670, 245-261, https://doi.org/10.1016/j.scitotenv.2019.03.177, 2019

1045 Jacquemart, M. and Tiampo, K.: Leveraging time series analysis of radar coherence and normalized
1046 difference vegetation index ratios to characterize pre-failure activity of the Mud Creek landslide,
1047 California, Nat. Hazards Earth Syst. Sci., 21, 629–642, https://doi.org/10.5194/nhess-21-629-2021,
1048 2021.

1049 Joyce, K.E., Belliss, S.E., Samsonov, S.V., McNeill, S.J. and Glassey, P.J.: A review of the status of
1050 satellite remote sensing and image processing techniques for mapping natural hazards and disasters.
1051 Prog. Phys. Geogr., 33~~(2)~~, 183-207, https://doi.org/10.1177/0309133309339563, 2009

1052 Jung, J. and Yun, S.H.: Evaluation of coherent and incoherent landslide detection methods based on
1053 Synthetic Aperture Radar for rapid response: A case study for the 2018 Hokkaido landslides. Remote
1054 Sens., 12~~(2)~~, 265, https://doi.org/10.3390/rs12020265, 2020

1055 Kennedy, R.E., Yang, Z., Gorelick, N., Braaten, J., Cavalcante, L., Cohen, W.B., Healey, S.:
1056 Implementation of the LandTrendr algorithm on google earth engine. Remote Sens. ~~(Basel)~~ 10, 691.
1057 https://doi.org/10.3390/rs10050691. 2018~~, 2018~~

1058 Kjekstad, O., Highland, L.: Economic and Social Impacts of Landslides. ~~In: Sassa, K., Canuti, P. (eds)~~
1059 Landslides – Disaster Risk Reduction. Sassa, K., Canuti, P. (eds), Springer, Berlin, Heidelberg.
1060 https://doi.org/10.1007/978-3-540-69970-5_30, 2009

1061 Konishi, T. and Suga, Y.: Landslide detection using COSMO-SkyMed images: A case study of a landslide
1062 event on Kii Peninsula, Japan. Eur. J. Remote Sens, 51~~(1)~~, 205-221,
1063 https://doi.org/10.1080/22797254.2017.1418185, 2018

1064 Komac M, Holley R, Mahapatra P, van der Marel H, Bavec M.: Coupling of GPS/GNSS and radar
1065 interferometric data for a 3D surface displacement monitoring of landslides. Landslides 12, 241–257,
1066 https://doi.org/10.1007/s10346-014-0482-0, 2015

1067 Korup, O., Densmore, A.L. and Schlunegger, F.: The role of landslides in mountain range evolution.
1068 Geomorphology, 120~~(1–2)~~, 77-90, https://doi.org/10.1016/j.geomorph.2009.09.017, 2010

1069 Kubwimana, D., Ait Brahim, L.~~A.~~, Nkurunziza, P., Dille, A., Depicker, A., Nahimana, L., Abdelouafi, A.
1070 and Dewitte, O.: Characteristics and Distribution of Landslides in the Populated Hillslopes of Bujumbura,
1071 Burundi. Geosci., 11~~(6)~~, 259, https://doi.org/10.3390/geosciences11060259, 2021

1072 Le Cozannet, G., Kervyn, M., Russo, S., Ifejika Speranza, C., Ferrier, P., Foumelis, M., Lopez, T.,
1073 Modaressi, H.: Space-Based Earth Observations for Disaster Risk Management. Surv. Geophys. 41,
1074 1209–1235, https://doi.org/10.1007/s10712-020-09586-5, 2020

Liu, C., Guo, L., Ye, L., Zhang, S., Zhao, Y. and Song, T.: A review of advances in China's flash flood early-warning system. Nat. Hazards 92, 619–634. https://doi.org/10.1007/s11069-018-3173-7, 2018

Marc, O., Stumpf, A., Malet, J.-P., Gosset, M., Uchida, T., and Chiang, S.-H.: Initial insights from a global database of rainfall-induced landslide inventories: the weak influence of slope and strong influence of total storm rainfall, Earth Surf. Dynam., 6, 903–922, https://doi.org/10.5194/esurf-6-903-2018, 2018.

Marengo, J.A. and Alves, L.M.: The 2011 intense rainfall and floods in Rio De Janeiro, Bulletin of the American Meteorological Society, 93~~(7)~~, 1-282~~pp.S1-S282~~, 2012

Martinis, S., Kuenzer, C., Wendleder, A., Huth, J., Twele, A., Roth, A. and Dech, S.: Comparing four operational SAR-based water and flood detection approaches. Int. J. Remote Sens., 36~~(13)~~, 3519-3543, https://doi.org/10.1080/01431161.2015.1060647, 2015

Mohan, A., Singh, A.K., Kumar, B. and Dwivedi, R.: Review on remote sensing methods for landslide detection using machine and deep learning. Trans. Emerg. Telecommun. Technol. T, 32~~(7)~~, 3998. https://doi.org/10.1002/ett.3998, 2021

Mondini, A.C.: Measures of spatial autocorrelation changes in multitemporal SAR images for event landslides detection. Remote Sens., 9~~(6)~~, 554, https://doi.org/10.3390/rs9060554, 2017

Mondini, A.C., Santangelo, M., Rocchetti, M., Rossetto, E., Manconi, A. and Monserrat, O.: Sentinel-1 SAR amplitude imagery for rapid landslide detection. Remote Sens., 11~~(7)~~, 760, https://doi.org/10.3390/rs11070760, 2019

Mondini, A.C., Guzzetti, F., Chang, K.T., Monserrat, O., Martha, T.R. and Manconi, A.: Landslide failures detection and mapping using Synthetic Aperture Radar: Past, present and future. Earth-Sci. Rev., 216, 103574, https://doi.org/10.1016/j.earscirev.2021.103574, 2021

Monsieurs, E., Jacobs, L., Michellier, C., Basimike Tchangaboba, J.~~B.~~, Bamulezi Ganza, G.~~B.~~, Kervyn, F., Maki Mateso, J.-C.~~M.~~, Mugaruka Bibentyo, T.~~M.~~, Kalikone Buzera, C.~~K.~~, Nahimana, L. Ndayisenga, A., Nkurunziza, P., Thiery, W., Demoulin, A., Kervyn M. and Dewitte, O.~~and Ndayisenga, A.~~: Landslide inventory for hazard assessment in a data-poor context: a regional-scale approach in a tropical African environment. Landslides, 15~~(11)~~, 2195-2209, https://doi.org/10.1007/s10346-018-1008-y, 2018a

Monsieurs, E., Kirschbaum, D.B., Tan, J., Maki Mateso, J.-C., Jacobs, L., Plisnier, P.-D., Thiery, W., Umutoni, A., Musoni, D., Mugaruka Bibentyo, T.~~M.~~ Bamulezi Ganza, G., Ilombe Mawe, G., Bagalwa, L., Kankurize, C., Michellier, C., Stanley, T., Kervyn, F., Kervyn, M., Demoulin, A., and Dewitte, O.~~and Ganza, G.B.~~: Evaluating TMPA rainfall over the sparsely gauged East African Rift. J. Hydrometeorol., 19~~(9)~~, 1507-1528, https://doi.org/10.1175/JHM-D-18-0103.1, 2018b

Monsieurs, E., Dewitte, O., and Demoulin, A.: A susceptibility-based rainfall threshold approach for landslide occurrence, Nat. Hazards Earth Syst. Sci., 19, 775–789, https://doi.org/10.5194/nhess-19-775-2019, 2019.

Monsieurs, E.: The potential of satellite rainfall estimates in assessing regional landslide hazard in Central Africa (Doctoral dissertation, Université de Liège, Liège, Belgium~~que~~), https://hdl.handle.net/2268/245576, 2020

Nakulopa, F., Vanderkelen, I., Van de Walle, J., Van Lipzig, N.P., Tabari, H., Jacobs, L., Tweheyo, C., Dewitte, O. and Thiery, W.: Evaluation of high-resolution precipitation products over the Rwenzori Mountains (Uganda). J. Hydrometeorol., 23, 747-768, https://doi.org/10.1175/JHM-D-21-0106.1, 2022

Nobile, A., Dille, A., Monsieurs, E., Basimike, J., Mugaruka Bibentyo, T.~~M.~~, d'Oreye, N., Kervyn, F. and Dewitte, O. Multi-temporal DInSAR to characterise landslide ground deformations in a tropical urban environment: Focus on Bukavu (DR Congo). Remote Sens., 10(4), ~~p.~~626, https://doi.org/10.3390/rs10040626, 2018

Nicholson, S. E.: Climate and climatic variability of rainfall over eastern Africa, Rev. Geophys., 5, 590–635, https://doi.org/10.1002/2016RG000544, 2017

NISAR, NASA-ISRO SAR (NISAR) Mission Science Users' Handbook. NASA Jet Propulsion Laboratory, 261, 18-1893., 2018

Nolan, M. and Fatland, D.R.: Penetration depth as a DInSAR observable and proxy for soil moisture. IEEE Trans. Geosci. Remote Sens., 41(3), 532-537, https://doi.org/10.1109/TGRS.2003.809931, 2003

d'Oreye, N., Derauw, D., Libert, L., Samsonov, S., *Dille, A., Nobile, A., *Monsieurs, E., Dewitte, O., Kervyn, F.: Automatization of InSAR mass processing using CSL InSAR Suite (CIS) software for Multidimensional Small Baseline Subset (MSBAS) analysis: example combining Sentinel-1 and Cosmo-SkyMed SAR data for landslides monitoring in South Kivu, DR Congo. ESA Living Planet Symposium 2019, Milano, Italy, 2019

d'Oreye, N., Derauw, D., Samsonov, S., Jaspard, M. and Smittarello, D.: MasTer: A Full Automatic Multi-Satellite InSAR Mass Processing Tool for Rapid Incremental 2D Ground Deformation Time Series. Int. Geosci. Remote Sens. Symp. (IGARSS), 1899-1902, https://doi.org/10.1109/IGARSS47720.2021.9553615, 2021

Park, S.E. and Lee, S.G.: On the use of single-, dual-, and quad-polarimetric SAR observation for landslide detection. ISPRS Int. J. Geo-Inf., 8(9), 384, https://doi.org/10.3390/ijgi8090384, 2019

Petersen, M.S.: Impacts of Flash Floods. ~~In: Gruntfest, E., Handmer, J. (eds)~~ Coping With Flash Floods. NATO Science Series, vol 77, Gruntfest, E., Handmer, J. (eds), Springer, Dordrecht. https://doi.org/10.1007/978-94-010-0918-8_2, 2001

Peterson, M., Mach, D., Buechler, D.: A Global LIS/OTD Climatology of Lightning Flash Extent Density. J. Geophys. Res. Atmos. 126. https://doi.org/10.1029/2020JD033885, 2021

Planet Team~~, 2017~~. Planet Application Program Interface: In Space for Life on Earth. San Francisco, CA. https://api.planet.com, 2017

Psomiadis, E.: October. Flash flood area mapping utilising SENTINEL-1 radar data, Earth Resour. Environ. Remote Sens./GIS App. VII, 10005, 100051G, https://doi.org/10.1117/12.2241055, 2016

Rengers, F.K., McGuire, L.A., Kean, J.W., Staley, D.M., Hobley, D.E.J.: Model simulations of flood and debris flow timing in steep catchments after wildfire. Water Resour. Res. 52, 6041–6061, https://doi.org/10.1002/2015WR018176, 2016.

Roback, K., Clark, M.K., West, A.J., Zekkos, D., Li, G., Gallen, S.F., Chamlagain, D. and Godt, J.W.: The size, distribution, and mobility of landslides caused by the 2015 Mw7. 8 Gorkha earthquake, Nepal. Geomorphology, 301, 121-138, https://doi.org/10.1016/j.geomorph.2017.01.030, 2018

Robinson, T.R., Rosser, N., Walters, R.J.: The Spatial and Temporal Influence of Cloud Cover on Satellite-Based Emergency Mapping of Earthquake Disasters. Sci. Rep. 9, 1–9. https://doi.org/10.1038/s41598-019-49008-0, 2019

Rocca, F., Prati, C., Monti Guarnieri, A., Ferretti, A.: SAR interferometry and its applications. Surv. Geophys. 21, 159–176. https://doi.org/10.1023/A:1006710731155, 2000

Samsonov, S., d'Oreye, N.: Multidimensional time-series analysis of ground deformation from multiple InSAR data sets applied to Virunga Volcanic Province. Geophys. J. Int. 191(3), 1095–1108. https://doi.org/10.1111/j.1365-246X.2012.05669.x, 2012

Scott, C.P., Lohman, R.B. and Jordan, T.E.: InSAR constraints on soil moisture evolution after the March 2015 extreme precipitation event in Chile. Sci. Rep., 7(1), 1-9. https://doi.org/10.1038/s41598-017-05123-4, 2017

Sekajugo, J., Kagoro-Rugunda, G., Mutyebere, R., Kabaseke, C., Namara, E., Dewitte, O., Kervyn, M., and Jacobs, L.: Can citizen scientists provide a reliable geo-hydrological hazard inventory? An analysis of biases, sensitivity and precision for the Rwenzori Mountains, Uganda, Environ. Res. Lett., 17, 045011, https://doi.org/10.1088/1748-9326/ac5bb5, 2022.

Shibayama, T., Yamaguchi, Y. and Yamada, H.: Polarimetric scattering properties of landslides in forested areas and the dependence on the local incidence angle. Remote Sens., 7(11), 15424-15442, https://doi.org/10.3390/rs71115424, 2015

Small, D.: Flattening gamma: Radiometric terrain correction for SAR imagery. IEEE Trans. Geosci. Remote Sens., 49(8), 3081-3093, https://doi.org/10.1109/TGRS.2011.2120616, 2011

Solari, L., Del Soldato, M., Raspini, F., Barra, A., Bianchini, S., Confuorto, P., Casagli, N. and Crosetto, M. Review of satellite interferometry for landslide detection in Italy. Rem. Sens., 12(8), p.1351. https://doi.org/10.3390/rs12081351, 2020

Srivastava, H.S., Patel, P. and Navalgund, R.R.: How far SAR has fulfilled its expectation for soil moisture retrieval. Microwave. Remote Sens. Atm. Env. 6410, 641001 https://doi.org/10.1117/12.693946, 2006

1176 Strozzi, T., Dammert, P.B., Wegmuller, U., Martinez, J.M., Askne, J.I., Beaudoin, A. and Hallikainen,
1177 N.T.: Landuse mapping with ERS SAR interferometry. IEEE Trans. Geosci. Remote Sens., 38(2), 766-
1178 775, https://doi.org/10.1109/36.842005, 2000

1179 Stumpf, A., Malet, J.P., Allemand, P. and Ulrich, P.: Surface reconstruction and landslide displacement
1180 measurements with Pléiades satellite images. ISPRS J. Photogramm. Remote Sens., 95, 1-12,
1181 https://doi.org/10.1016/j.isprsjprs.2014.05.008, 2014

1182 Tessari, G., Floris, M. and Pasquali, P.: Phase and amplitude analyses of SAR data for landslide detection
1183 and monitoring in non-urban areas located in the North-Eastern Italian pre-Alps. Environmental Earth
1184 Sciences, 76(2), 85, https://doi.org/10.1007/s12665-017-6403-5, 2017

1185 Thiery, W., Davin, E.L., Panitz, H.-J., Demuzere, M., Lhermitte, S., van Lipzig, N.P.M.: The impact of
1186 the African Great Lakes on the regional climate, J. Climate, 28(10), 4061-4085,
1187 https://doi.org/10.1175/JCLI-D-14-00565.1, 2015.

1188 Thiery, W., Davin, E.L., Seneviratne, S.I., Bedka, K., Lhermitte, S., van Lipzig, N.P.M.: Hazardous
1189 thunderstorm intensification over Lake Victoria, Nat. Comm., 7, 12786,
1190 https://doi.org/10.1038/ncomms12786, 2016

1191 Thiery, W., Gudmundsson, L., Bedka, K., Semazzi, F.H.M., Lhermitte, S., Willems, P., van Lipzig, N.P.M.,
1192 Seneviratne, S.I.: Early warnings of hazardous thunderstorms over Lake Victoria, Env. Res. Lett,
1193 12, 074012, https://doi.org/10.1088/1748-9326/aa7521, 2017

1194 Truong, C., Oudre, L. and Vayatis, N.: Selective review of offline change point detection methods. Signal
1195 Process., 167, 107299, https://doi.org/10.1016/j.sigpro.2019.107299, 2020

1196 Tucker, C.J.: Red and photographic infrared linear combinations for monitoring vegetation. Remote
1197 Sens. Environ. 8, 127–150. https://doi.org/10.1016/0034- 4257(79)90013-0, 1979

1198 Turkington, T., Ettema, J., van Westen, C. J., and Breinl, K.: Empirical atmospheric thresholds for debris
1199 flows and flash floods in the southern French Alps, Nat. Hazards Earth Syst. Sci., 14, 1517–1530,
1200 https://doi.org/10.5194/nhess-14-1517-2014, 2014.

1201 Twele, A., Cao, W., Plank, S. and Martinis, S.: Sentinel-1-based flood mapping: a fully automated
1202 processing chain. Int. J. Remote Sens., 37(13), 2990-3004,
1203 https://doi.org/10.1080/01431161.2016.1192304, 2016

1204 Tzouvaras, M., Danezis, C. and Hadjimitsis, D.G.: Small scale landslide detection using Sentinel-1
1205 interferometric SAR coherence. Remote Sens., 12(10), 1560, https://doi.org/10.3390/rs12101560,
1206 2020

1207 Ulaby, F.T., Dubois, P.C. and Van Zyl, J.: Radar mapping of surface soil moisture. J. Hydrol., 184(1-2),
1208 57-84, https://doi.org/10.1016/0022-1694(95)02968-0, 1996

Van de Walle, J., ~~onas~~, ~~Wim~~ Thiery, W., ~~Oscar~~ Brousse, O., ~~Niels~~ Souverijns, N., ~~Matthias~~ Demuzere, M., and ~~Nicole PM~~ van Lipzig, N.P.M.~~.~~: A convection-permitting model for the Lake Victoria Basin: Evaluation and insight into the mesoscale versus synoptic atmospheric dynamics. Clim. Dyn., 54 ~~(3)~~, 1779-1799. https://doi.org/10.1007/s00382-019-05088-2, 2020

van Westen, C.J., ~~;~~ Castellanos, E., ~~;~~ Kuriakose, S.L.: Spatial data for landslide susceptibility, hazard, and vulnerability assessment: An overview. Eng. Geol. 2008, 102, 112–131, https://doi.org/10.1016/j.enggeo.2008.03.010, 2008

Weydahl, D.J.: Analysis of ERS SAR coherence images acquired over vegetated areas and urban features. Int. J. Remote Sens., 22 ~~(14)~~, 2811-2830, https://doi.org/10.1080/01431160010006412, 2001

Zebker, H.A. and Villasenor, J.: Decorrelation in interferometric radar echoes. IEEE Trans. Geosci. Remote Sens., 30 ~~(5)~~, 950-959, https://doi.org/10.1109/36.175330, 1992

Zhong, C., Li, C., Gao, P. and Li, H.: Discovering Vegetation Recovery and Landslide Activities in the Wenchuan Earthquake Area with Landsat Imagery. Sensors, 21 ~~(15)~~, 5243, https://doi.org/10.3390/s21155243, 2021